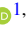# Numerical simulation of dynamics behavior of pulsed-DC helium plasma jet confined by parallel magnetic field at atmospheric pressure

Yinghua Liu [1,2] Peiqi Yin,[1,2] Boping Xu [1,2] Dawei Liu,[3] Liangwen Pi,[2,4] Yuxi Fu,[2,4]
Yishan Wang,[1,2] Wei Zhao,[1,2] and Jie Tang [1,2,*]

[1]*State Key Laboratory of Transient Optics and Photonics, Xi'an Institute of Optics and Precision Mechanics of CAS,
Xi'an, Shaanxi 710119, People's Republic of China*
[2]*University of Chinese Academy of Sciences, Beijing 100049, People's Republic of China*
[3]*State Key Laboratory of Advanced Electromagnetic Technology, School of Electrical and Electronic Engineering,
Huazhong University of Science and Technology, Wuhan, Hubei 430074, People's Republic of China*
[4]*Center for Attosecond Science and Technology, Xi'an Institute of Optics and Precision Mechanics of CAS,
Xi'an, Shaanxi 710119, People's Republic of China*

A two-dimensional axisymmetric fluid model is used to simulate the dynamics behavior of an atmospheric-pressure helium plasma jet in the presence of a parallel magnetic field. The plasma jet is generated in a coaxial dielectric barrier discharge (DBD) driven by pulsed direct-current voltage. Comparative analysis of the plasma jet with and without the parallel magnetic field indicates that a slightly thinner plasma sheath inside the tube is present with the parallel magnetic field as a result of the decreased accumulated electrons on the inner surface of dielectric tube. After the streamer propagates outside the tube, a little more concentrated electron distribution in the annular wall is observed by applying the magnetic field because of the reduced electron diffusion in the radial direction and the confinement effect of the magnetic field on the electrons in the avalanche heads. The tiny reduction in the length of plasma jet is attributed to the $E \times B$ drift of charged particles. These results demonstrate that the parallel magnetic field has no apparent effect on the propagation of the plasma jet, and it contributes little to the performance improvement of the coaxial DBD, which agrees well with the previous experimental observations. This little impact of the parallel magnetic field on the coaxial DBD plasma jet may result from negligible contribution of the memory effect to the sole discharge pulse as well as the weak confinement effect of the applied magnetic field on the surface electrons that moves along the magnetic field lines under electrostatic repulsion.

I. INTRODUCTION

The atmospheric-pressure plasma jet (APPJ) has become one of the hot spots in the field of plasma research in recent decades because of its broad application prospects in material processing and biomedicine [1–6]. Compared with other plasma devices, the plasma jet can deliver abundant active species from narrow gas gaps to open spaces and can be used to treat samples with various shapes and sizes [7–9]. APPJs can be generated by direct-current (DC) discharges [10–17]. For example, Duan *et al.* [10] and Tang *et al.* [11] designed brush-shaped plasma jets based on DC glow discharge. Fridman *et al.* [12] and Shiki *et al.* [13] developed torchlike plasma jets by gliding-arc discharge. To improve the working efficiency of APPJs in industrial and medical applications,

introduction of the magnetic field to plasmas has been proposed. Feng *et al.* [16] found that the length of the plasma torch (19 cm) was increased by ∼3 times, and the adhesion of the treated polymer films was improved by up to ∼30 times, after applying a magnetic field (0.25 T) perpendicular to the electric field. Jiang *et al.* [17] reported a 34% reduction in the total energy consumption for plasma generation, 40% increment in the jet length, and more than twofold enhancement in the irradiance with the application of a perpendicular magnetic field (0.42 T), accompanied by the notable improvement in the uniformity of the plasma brush. The improvement of DC discharge by the perpendicular magnetic field is attributed to the enhanced ionization and excitation process in the curved and lengthened electron path due to the Lorentz force as well as the same direction of $E \times B$ drift as the gas flow.

Dielectric barrier discharge (DBD) is regarded as another common way to generate APPJs because of its simpler electrode configuration and lower power consumption than DC discharge [6,8,18,19]. In addition to the perpendicular magnetic field used to optimize DC discharges, a magnetic field parallel to the electric field was also capable of improving the discharge intensity and uniformity significantly at atmospheric pressure, where the plasma was produced between

*Contact author: tangjie@opt.ac.cn

two parallel-plate electrodes in a repetitive unipolar nanosecond pulsed DBD [20–22]. The authors believed that the enhancement of the memory effect and the confinement of the magnetic field on electrons are the main reasons for the discharge improvement. Additionally, many streamerlike plasma jets have been developed in coaxial DBDs [23–30]. However, it has been demonstrated in several studies that the coaxial DBD APPJs are not sensitive to the parallel magnetic fields. Liu *et al.* [27] employed ring permanent magnets to produce a parallel magnetic field of 0.587 T in the region of a helium APPJ, and little effect was measured for the free expanding plasma plumes. Shi *et al.* [28] showed that the growth in the length and irradiance of a helium plasma jet was closely related to the position of the magnetic ring. The growth was inconspicuous with the magnetic ring placed downstream of the high-voltage electrode. A 40% improvement in APPJ length and a 23% increase in the intensity of spectral line O (777.2 nm) were acquired only when the magnetic ring moved to the periphery of the high-voltage electrode.

The above experiments show that the parallel magnetic field generally has little impact on the APPJs produced by coaxial DBDs, which is quite different from the great improvement of discharge performance observed in both DC discharges and parallel-plate DBDs. It has been reported that this little impact on the APPJs probably lies in the fact that the electron collision frequency is much more than the electron cyclotron frequency, and collisions make the magnetoactive collisional plasmas isotropic for transport when using a magnetic field on the order of a few tenths of a Tesla at atmospheric pressure [27]. Nevertheless, the reason why the parallel magnetic field contributes little to the coaxial DBDs has not been clearly addressed, and the influence mechanism of the parallel magnetic field on the APPJs has not been fully clarified in coaxial DBDs. For instance, the motion manner and drift trajectory of an electron under the action of parallel magnetic fields is still unclear. Moreover, the variation of microscopic characteristics of APPJs in the parallel magnetic field has not yet been systematically discussed in coaxial DBDs. These deficiencies prevent further understanding of the characteristics of a plasma jet confined by a magnetic field and bring blindness to the working optimization of a magnetic-field-assisted plasma jet.

Furthermore, a similar experiment was conducted by placing the ring magnets downstream of the power electrode in a coaxial DBD [29], and it came to an exciting conclusion that the parallel magnetic field (ranges from 0.1 to 0.4 T) had an apparently positive impact on the streamer discharge, where the length and brightness of the APPJs were significantly enhanced. Additionally, a parallel magnetic field (0.2 T) generated by a pair of Helmholtz coils was applied to the coaxial DBD argon plasma jet [30]. Examination of the plasma physical appearance and optical emission indicated that the plasma irradiance was increased. These experimental observations are quite distinct from the reports mentioned above. That is to say, an inconsistence about the enhancement effect of parallel magnetic field on coaxial DBDs comes into being. However, theoretical reports are lacking that verify these published experimental results and clarify this academic disagreement.

Based on the above considerations, it is necessary and essential to fully and deeply explore and understand the complicated dynamic behavior of plasma jets during the overall discharge process in the presence of the parallel magnetic field. At present, due to the limitation of experimental diagnostic techniques, the spatiotemporal distributions of electrons, ions, and electric fields in the discharge space cannot be well examined and understood. Here, a two-dimensional axisymmetric self-consistent model of pulsed-DC driving an APPJ is developed with a parallel magnetic field applied. All efforts of this work will allow us to gain further insight into the intrinsic mechanism of the effect of a magnetic field on plasma jets, to reach a common understanding and recognition on the enhancement effect of magnetic field on plasma jets, and to avoid the poorly efficient generation of plasmas and the lowly effective utilization of plasma jets with the magnetic field applied in various applications.

II. MODEL

A two-dimensional axisymmetric self-consistent fluid model is established according to the previous relevant experiments [27–30] and used to simulate the influence of the steady magnetic field on a coaxial DBD APPJ. Figure 1(a) depicts the schematic diagram of the simulation geometry, which is built in an axisymmetric cylindrical coordinate (r, z). Only the left half of the computational domain is shown, and the boundary AG is the symmetric axis. In this paper, pure helium gas flows through a dielectric tube (length of 5 mm, inner diameter of 2 mm, and outer diameter of 16 mm) and merges into the ambient air. The air is composed of 80% nitrogen and 20% oxygen in the model. The helium flow rate is constant as 2 standard liter per minute (SLM), which is equal to a mean inlet velocity of 10.61 m/s. Two permanent ring magnets (recoil permeability of 1.05 and remanent magnetic flux density norm of 1.41 T) are stacked downstream of the dielectric tube with the N pole close to the dielectric tube and the S pole far away from the dielectric tube. Each ring magnet has an inner diameter of 16 mm, an outer diameter of 28 mm, and a height of 4 mm. The APPJ is driven by pulsed-DC high voltage (HV) with an amplitude of 4 kV and a rise time of 50 ns. The HV ring electrode (length of 2 mm, inner diameter of 4 mm, and outer diameter of 4.4 mm) is embedded in the dielectric tube (relative permittivity of 5) in a coaxial manner. The gas discharge mainly occurs in the smaller domain (ACFG), which is depicted on both sides of the symmetric axis, as shown in Fig. 1(b). The boundaries CF and FG are grounded, as indicated by the green solid lines. Figure 1(c) shows the spatial distribution of the stationary electric field with the 4 kV voltage applied to the ring electrode, not considering the field distortion by the plasma. Without the consideration of the process of generating plasma by gas discharge, the stationary electric field is solved by calculating the Laplacian equation $\nabla \cdot \boldsymbol{E} = 0$. The strongest electric field of 8.2×10^5 V/m within the investigated domain is obtained near the dielectric inner surface downstream of the power electrode, from which the electric field inside the tube gradually weakens toward both ends of the tube on the whole. This stationary electric field outside the tube reaches its maximum value approaching the corner of tube exit and decreases in the direction away from the tube exit.
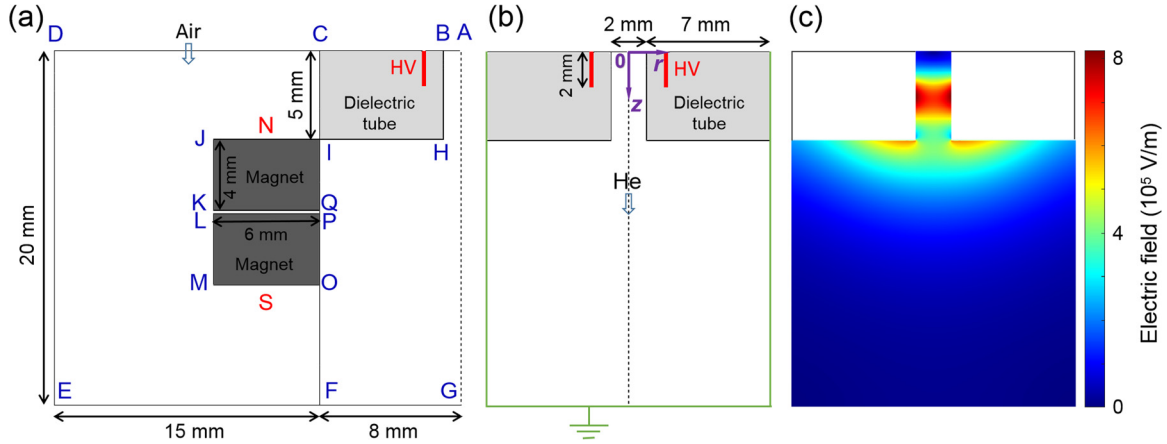
FIG. 1. (a) Schematic diagram of simulation geometry. AG: Symmetric axis; AB: Inlet for helium gas; BHICB: Boundary of the dielectric tube; IQKJI: Boundary of ring magnet; POMLP: Boundary of another ring magnet; CD: Inlet for air; DE and EG: Outlet for gas species; N: N pole of the ring magnet; S: S pole of the ring magnet. (b) Detail of the gas discharge region. Red rectangular area: High-voltage (HV) ring electrode. Green lines: Grounded electrode. (c) The spatial distribution of stationary electric field with the 4 kV voltage applied to the ring electrode.

For the plasma jet generated by pulsed DC discharge, since the propagation speed of the streamer ($\sim 10^5$ m/s) is much higher than the gas flow rate (~ 10 m/s), the gas spreads out a negligible distance in the investigated time span, and the temporal and spatial profiles of mole fraction remain unchanged [31,32]. As a result, the overall problem is divided into three components: a steady neutral gas flow component, a magnetic field component, and a transient plasma dynamics component. The larger domain (ADEG) is used for the neutral gas flow and the magnetic field components, while the smaller domain (ACFG) is used for the plasma dynamics component.

A. Neutral gas flow model

The governing equations of the neutral gas flow model consist of the continuity equation [Eq. (1)], the momentum conservation (Navier-Stokes) equation [Eq. (2)], and the convection-diffusion equation [Eq. (3)] [32,33]:

$$\nabla \cdot (\rho \boldsymbol{u}) = 0, \tag{1}$$

$$(\nabla \cdot \rho \boldsymbol{u}\boldsymbol{u}) = -\nabla p - (\nabla \cdot \tau) + \boldsymbol{F}, \tag{2}$$

$$\nabla \cdot (\rho \boldsymbol{u} w_g) + \nabla \cdot \boldsymbol{J}_g = 0, \tag{3}$$

where ρ is the mixture density (helium 0.1664 kg m^{-3}, air 1.293 kg m^{-3}), $\boldsymbol{u}$ is the velocity vector, p is the pressure, τ is the stress tensor for a Newtonian fluid, $\boldsymbol{F}$ is the body force, w is the mass fraction, and the subscript g represents the species of gases (i.e., He and air). For laminar flow, the diffusion flux $\boldsymbol{J}_g = -\rho D_g \nabla w_g$, where D_g is the binary molecular diffusion coefficient (helium in air 7.2×10^{-5} m^2 s^{-1}). The boundary conditions for the neutral gas flow model are summarized in Table I. The corresponding boundaries can be found in Fig. 1(a).

B. Magnetic field model

The magnetic flux density $\boldsymbol{B}$ is governed by Gauss's law for magnetic fields [Eq. (4)], Ampere's law [Eq. (5)], and the

constitutive relations [Eqs. (6) and (7)]:

$$\nabla \cdot \boldsymbol{B} = 0, \tag{4}$$

$$\boldsymbol{H} = -\nabla V_m, \tag{5}$$

$$\boldsymbol{B} = \mu_0 \mu_{\text{rec}} \boldsymbol{H} + \boldsymbol{B}_R$$

(in the regions of the two ring magnets), $\qquad$ (6)

$$\boldsymbol{B} = \mu_0 \mu_r \boldsymbol{H}$$

(in the regions of the flowing gas and dielectric tube), (7)

where $\boldsymbol{H}$ is the magnetic field strength, V_m is the magnetic scalar potential, μ_0 is the vacuum magnetic permeability, μ_{rec} is the recoil permeability of the two permanent ring magnets (constant as 1.05), $\boldsymbol{B}_R$ is the remanent magnetic flux density of the two permanent ring magnets (1.41 T, along the reverse direction of the z axis), and μ_r is the relative permeability in the regions of the flowing gas and dielectric tube (set to 1). The boundary conditions for the magnetic field model are summarized in Table II.

C. Plasma dynamics model

The plasma dynamics component solves the Poisson equation [Eq. (8)], the species continuity equations [Eq. (9)], and the electron energy conservation equation [Eq. (11)] [31–34]:

$$-\varepsilon_0 \nabla \cdot (\varepsilon_r \nabla \Phi) = \varepsilon_0 \nabla \cdot (\varepsilon_r \boldsymbol{E}) = \sum_k q_k n_k, \tag{8}$$

$$\frac{\partial n_k}{\partial t} + \nabla \cdot \boldsymbol{\Gamma}_k = R_k, \tag{9}$$

$$\boldsymbol{\Gamma}_k = \text{sgn}(q_k) n_k \mu_k \boldsymbol{E} - D_k \nabla n_k, \tag{10}$$

$$\frac{\partial n_\varepsilon}{\partial t} + \nabla \cdot \left(\frac{5}{3} \mu_e \boldsymbol{E} n_\varepsilon - \frac{5}{3} D_e \nabla n_\varepsilon \right)$$

$$= -e\boldsymbol{\Gamma}_e \cdot \boldsymbol{E} - \sum_j \Delta E_j K_{\text{inel},j} - 3\frac{m_e}{M} k_b n_e v_{\text{en}}(T_e - T_g), \tag{11}$$

TABLE I. The computational boundary condition for the neutral gas flow model.

	AB	CD	BHIC	IQKJI	POMLP	DE	EG
u_r	0	0	0	0	0	$\frac{\partial u_r}{\partial r} - \frac{1}{3}(\nabla \cdot \boldsymbol{u}) = 0$	0
u_z	10.61 m/s	0.3 m/s	0	0	0	0	$\frac{\partial u_z}{\partial z} - \frac{1}{3}(\nabla \cdot \boldsymbol{u}) = 0$
w_{He}	1	0	$\nabla w_{\text{He}} \cdot \boldsymbol{n} = 0$	$\nabla w_{\text{He}} \cdot \boldsymbol{n} = 0$	$\nabla w_{\text{He}} \cdot \boldsymbol{n} = 0$	$\frac{\partial w_{\text{He}}}{\partial r} = 0$	$\frac{\partial w_{\text{He}}}{\partial z} = 0$
w_{air}	0	1	$\nabla w_{\text{air}} \cdot \boldsymbol{n} = 0$	$\nabla w_{\text{air}} \cdot \boldsymbol{n} = 0$	$\nabla w_{\text{air}} \cdot \boldsymbol{n} = 0$	$\frac{\partial w_{\text{air}}}{\partial r} = 0$	$\frac{\partial w_{\text{air}}}{\partial z} = 0$

Note: u_r and u_z are the velocity components in the radial and axial direction, respectively. $\boldsymbol{n}$ is the unit normal vector pointing towards the boundary.

where ε_0 is the vacuum permittivity, ε_r is the relative permittivity of the dielectric material, Φ is the electric potential, $\boldsymbol{E}$ represents the electric field, q is the charge, n is the number density, the subscript k indicates the kth species included in the plasma chemistry, $\boldsymbol{\Gamma}$ is the species number flux in the drift-diffusion approximation, R_k is the source term for the kth species, $\text{sgn}(q_k)$ is the sign function (positive or negative), μ is the mobility, D is the diffusion coefficient, n_ε is the electron energy density, the subscript e represents the electrons, e is the electron charge, the subscript j denotes the jth reaction, and ΔE and K_{inel} are the energy loss during the inelastic collisions and the corresponding reaction rate, respectively. Here, m_e, M, k_b, and v_{en} are electron mass, gas species mass, the Boltzmann constant, and the electron-neutral momentum transfer collision frequency, respectively. Also, T_e is the electron temperature. The gas temperature T_g is 300 K.

The diffusion coefficients of all species except electrons are computed using a mixture-average formulation. The mixture-averaged diffusion coefficient of species k is defined as $D_k = \frac{1-\omega_k}{\sum_{j\neq k} x_j/D_{kj}}$, where ω_k is the mass fraction of species k; x_j is the mole fraction of species j; and D_{kj} is the binary diffusion coefficient between species k and j. The latter is calculated using the Chapman-Enskog theory [35,36] and depends on Lennard-Jones binary interaction potential parameters. It is assumed that the Lennard-Jones coefficients used to calculate the D_{kj}'s of ions and excited species equal the ones used for the ground-state neutrals. Therefore, the diffusion coefficient of an ionic or excited species is equal to the diffusion coefficient of its ground-state neutral counterpart. The mobility of ions is computed based on Einstein's relation $\mu_i = q_i D_i / k_b T_i$, where the subscript i stands for ions. The ion temperature T_i equals the gas temperature by assuming all ions and neutrals in thermal equilibrium with each other. For the neutral species, the mobility is set equal to zero.

Table III summarizes the boundary conditions for the plasma dynamics model. The boundary conditions for the particle number flux ($\boldsymbol{\Gamma}_e$, $\boldsymbol{\Gamma}_i$, and $\boldsymbol{\Gamma}_m$) and the electron energy

TABLE II. The computational boundary condition for the magnetic field model.

	ABCD	DE	EFG	A
V_m	$\frac{\partial V_m}{\partial z} = 0$	$\frac{\partial V_m}{\partial r} = 0$	$\frac{\partial V_m}{\partial z} = 0$	0

flux ($\boldsymbol{\Gamma}_\varepsilon$) at the solid walls are set as follows:

$$\boldsymbol{n} \cdot \boldsymbol{\Gamma}_e = \frac{1}{4} n_e \sqrt{\frac{8 k_b T_e}{\pi m_e}} - \alpha_s \sum_i \gamma_i (\boldsymbol{\Gamma}_i \cdot \boldsymbol{n}) + \alpha_s' \mu_e n_e \boldsymbol{E}, \quad (12)$$

$$\boldsymbol{n} \cdot \boldsymbol{\Gamma}_i = \frac{1}{4} n_i \sqrt{\frac{8 k_b T_i}{\pi m_i}} + \alpha_s \mu_i n_i \boldsymbol{E}, \quad (13)$$

$$\boldsymbol{n} \cdot \boldsymbol{\Gamma}_m = \frac{\gamma_m}{1 - \gamma_m/2} \frac{1}{4} n_m \sqrt{\frac{8 k_b T_g}{\pi m_m}}, \quad (14)$$

$$\boldsymbol{n} \cdot \boldsymbol{\Gamma}_\varepsilon = \frac{1}{2} n_\varepsilon \sqrt{\frac{8 k_b T_e}{\pi m_e}} - \alpha_s 2 k_b T_e \sum_i \gamma_i (\boldsymbol{\Gamma}_i \cdot \boldsymbol{n}), \quad (15)$$

where $\boldsymbol{n}$ is the unit vector pointing toward the solid wall, and the subscripts m and ε stand for the metastables and the electron energy, respectively. Here, m_i is the ion mass, and m_m is the mass of metastables. The secondary electron emission coefficient γ_i is set as 0.1 for all positive ions, which means the dielectric surface is supposed to emit secondary electrons under ion bombardment. The sticking coefficient γ_m is set as 1 for all excited neutrals, radicals, and ion species, which means that all excited species, radicals, and ions that impact wall surfaces are assumed to return to the gas phase as their corresponding ground-state neutrals. Also, α_s and α_s' are switching functions depending on the dot product of $\boldsymbol{E}$ and $\boldsymbol{n}$:

$$\alpha_s = \begin{cases} 1 & (\boldsymbol{E} \cdot \boldsymbol{n} \geqslant 0) \\ 0 & (\boldsymbol{E} \cdot \boldsymbol{n} < 0) \end{cases}, \; \alpha_s' = \begin{cases} 0 & (\boldsymbol{E} \cdot \boldsymbol{n} \geqslant 0) \\ 1 & (\boldsymbol{E} \cdot \boldsymbol{n} < 0) \end{cases}. \quad (16)$$

The electric potential on the dielectric material is obtained from Gauss's law:

$$(\boldsymbol{D}_2 - \boldsymbol{D}_1) \cdot \boldsymbol{n} = \sigma_s, \; \frac{d\sigma_s}{dt} = \boldsymbol{J}_i \cdot \boldsymbol{n} + \boldsymbol{J}_e \cdot \boldsymbol{n}, \quad (17)$$

where $\boldsymbol{D}_1$ and $\boldsymbol{D}_2$ are the electric displacement vectors, σ_s is the net charge density accumulated on the dielectric surface, and $\boldsymbol{J}_i$ and $\boldsymbol{J}_e$ are the total ion current density and the electron current density on the surface, respectively.

When a steady magnetic field is introduced to the plasma dynamics model, the mobility and diffusion coefficient of charged particles are transformed into tensors [30]. The following expressions in Eqs. (18) and (19) for electron mobility tensor correspond to the case where the magnetic field is in

TABLE III. The computational boundary condition for the plasma dynamics model.

	AB	BC	CI	IF	FG	BHI	Ring
n_e	$\frac{\partial n_e}{\partial z} = 0$	…	…	$\frac{\partial n_e}{\partial r} = 0$	Eq. (12)	Eq. (12)	…
n_i	$\frac{\partial n_i}{\partial z} = 0$	…	…	$\frac{\partial n_i}{\partial r} = 0$	Eq. (13)	Eq. (13)	…
n_m	$\frac{\partial n_m}{\partial z} = 0$	…	…	$\frac{\partial n_m}{\partial r} = 0$	Eq. (14)	Eq. (14)	…
n_ε	$\frac{\partial n_\varepsilon}{\partial z} = 0$	…	…	$\frac{\partial n_\varepsilon}{\partial r} = 0$	Eq. (15)	Eq. (15)	…
Φ	$\frac{\partial \Phi}{\partial z} = 0$	$\frac{\partial \Phi}{\partial z} = 0$	0	0	0	Eq. (17)	Φ_a

Note: The boundary ring represents the HV electrode. Φ_a is the applied voltage.

the z (axial) and r (radial) directions:

$$\mu_e' = \frac{1}{1 + \mu_e^2 B_z^2} \begin{bmatrix} \mu_e & -B_z\mu_e^2 & 0 \\ B_z\mu_e^2 & \mu_e & 0 \\ 0 & 0 & \mu_e(1 + \mu_e^2 B_z^2) \end{bmatrix}$$

$$= \begin{bmatrix} \frac{ev_m}{m_e(v_m^2+\omega_c^2)} & -\frac{e\omega_c}{m_e(v_m^2+\omega_c^2)} & 0 \\ \frac{e\omega_c}{m_e(v_m^2+\omega_c^2)} & \frac{ev_m}{m_e(v_m^2+\omega_c^2)} & 0 \\ 0 & 0 & \frac{e}{m_e v_m} \end{bmatrix}, \quad (18)$$

$$\mu_e' = \frac{1}{1 + \mu_e^2 B_r^2} \begin{bmatrix} \mu_e(1 + \mu_e^2 B_r^2) & 0 & 0 \\ 0 & \mu_e & -B_r\mu_e^2 \\ 0 & B_r\mu_e^2 & \mu_e \end{bmatrix}$$

$$= \begin{bmatrix} \frac{e}{m_e v_m} & 0 & 0 \\ 0 & \frac{ev_m}{m_e(v_m^2+\omega_c^2)} & -\frac{e\omega_c}{m_e(v_m^2+\omega_c^2)} \\ 0 & \frac{e\omega_c}{m_e(v_m^2+\omega_c^2)} & \frac{ev_m}{m_e(v_m^2+\omega_c^2)} \end{bmatrix}, \quad (19)$$

where μ_e is the electron mobility in the absence of a magnetic field (0.1132 $\text{m}^2\,\text{V}^{-1}\,\text{s}^{-1}$ in our model). Here, B_r and B_z are the radial and axial components of the magnetic flux density, respectively. The total electron collision frequency is expressed as $v_m = n \cdot v_e \cdot Q_m$, where n is gas number density, v_e is the electron velocity, and Q_m is electron momentum transfer cross-section [37]. The electron cyclotron angular frequency $\omega_c = eB/m_e$, where B is the magnetic flux density. The diffusion coefficient of the electrons in the presence of a magnetic field is calculated using Einstein's relation as follows:

$$D_e' = \frac{k_b T_e}{e} \mu_e'. \quad (20)$$

It can be concluded that the mobility and diffusion coefficients in the direction perpendicular to the magnetic field are reduced to $1/(1 + \beta^2)$ of those in the absence of the magnetic field ($\beta = \omega_c/v_m$ is the Hall parameter) [38].

D. Plasma chemistry

All reactions and corresponding rate coefficients are listed in Table IV. The helium-air chemistry set is determined by referring to the previously published paper [33,46–48]. Compared with the recent simulation study on pulsed microwave discharge in pure N_2 [49], the reaction mechanism for N_2 is rationally simplified in this paper based on the principle of compromise between short calculation time and high calculation accuracy [50–52]. The following particles are considered in the plasma chemistry: the gas molecules in the ground state (He, N_2, and O_2), the electrons (e), the ions (He$^+$, He$_2^+$, N$_2^+$,

O$_2^+$, O$_2^-$, and O$^-$), oxygen atoms [O in the ground state and O(^{1}D) in the excited state], the metastable helium molecules [He* which represents He(2^1S) and He(2^3S) and He$_2^*$ which represents He$_2$(a$^3\Sigma_u^+$)], vibrationally excited air molecules [N$_2$($\nu = 1$), N$_2$($\nu = 3$), N$_2$($\nu = 4$), N$_2$($\nu = 5$), O$_2$($\nu = 3$), and O$_2$($\nu = 4$)], electronically excited air molecules [N$_2$(A$^3\Sigma_u^+$), O$_2$(a$^1\Delta_g$), O$_2$(b$^1\Sigma_g^+$), and O$_2$(A$^3\Sigma_u^+$, C$^3\Delta_u$, c$^1\Sigma_u^-$)]. For the elastic collision (R1 and R4), electron impact excitation (R2, R5–R9, R11–R18, R20, and R21), electron impact ionization (R3, R10, and R22), and electron attachment reaction (R19), their reaction rates are calculated using BOLSIG+ [39] with the cross-section data from the LXCat database [40–42]. Here, the Maxwellian assumption is taken for electron energy distribution function [33,53]. It should be noted that photoionization is not considered in our model. Instead, a uniform background electron density of 10^{13} m^{-3} is predefined in the discharge space to supply the initial seed electrons for the propagation of ionization wave [32,33].

E. Numerical implementation

In this paper, COMSOL Multiphysics software version 5.3 is used for the simulation [54]. First, Eqs. (1)–(7) are solved to obtain the steady-state fluid velocity and pressure, mole fraction, and magnetic flux density profiles. These results are then used as the initial condition for Eqs. (8)–(11) to acquire the time-dependent charged and minority neutral species concentrations as well as the electric field profiles. All governing equations are discretized in space by using the continuous Galerkin finite element method with the free triangle meshes. To describe the complicated chemical reaction in the helium-air mixed layer, the maximum mesh size is set to 0.04 mm inside the tube and in the region $r < 1.5$ mm outside the tube. The remaining region is more sparsely meshed with the maximum mesh size of 0.2 mm. The complete mesh consists of $\sim 8 \times 10^4$ cells, and the total number of degrees of freedom is $\sim 7 \times 10^5$.

In the stationary computations, Eqs. (1)–(7) are distributed into three groups by using a segregated solver. For the first group, P1-P1 discretization is applied, which means that piecewise linear interpolation shape functions are used for both velocity and pressure field. For the second group, the concentration field is discretized using linear Lagrange elements. For the third group, quadratic Lagrange elements are used for the magnetic field. The first and second groups are strongly coupled by the velocity vector. The streamline diffusion and crosswind diffusion options are activated for stability in these two groups. Within each segregated

TABLE IV. List of reactions included in this study.

No.	Reaction	Rate coefficient	Activation energy	Reference
R1	$e + He \rightarrow e + He$	BOLSIG+	0	[39,40]
R2	$e + He \rightarrow e + He^*$	BOLSIG+	19.8	[39,40]
R3	$e + He \rightarrow 2e + He^+$	BOLSIG+	24.6	[39,40]
R4	$e + N_2 \rightarrow e + N_2$	BOLSIG+	0	[39,41]
R5	$e + N_2 \rightarrow e + N_2(\nu = 1)$	BOLSIG+	0.2889	[39,41]
R6	$e + N_2 \rightarrow e + N_2(\nu = 3)$	BOLSIG+	0.8559	[39,41]
R7	$e + N_2 \rightarrow e + N_2(\nu = 4)$	BOLSIG+	1.134	[39,41]
R8	$e + N_2 \rightarrow e + N_2(\nu = 5)$	BOLSIG+	1.409	[39,41]
R9	$e + N_2 \rightarrow e + N_2(A^3\Sigma_u^+)$	BOLSIG+	6.17	[39,40]
R10	$e + N_2 \rightarrow 2e + N_2^+$	BOLSIG+	15.6	[39,41]
R11	$e + O_2 \rightarrow e + O_2(\nu = 3)$	BOLSIG+	0.57	[39,42]
R12	$e + O_2 \rightarrow e + O_2(\nu = 4)$	BOLSIG+	0.772	[39,42]
R13	$e + O_2 \rightarrow e + O_2(a^1\Delta_g)$	BOLSIG+	0.977	[39,42]
R14	$e + O_2(a^1\Delta_g) \rightarrow e + O_2$	BOLSIG+	−0.977	[39,42]
R15	$e + O_2 \rightarrow e + O_2(b^1\Sigma_g^+)$	BOLSIG+	1.627	[39,42]
R16	$e + O_2(b^1\Sigma_g^+) \rightarrow e + O_2$	BOLSIG+	−1.627	[39,42]
R17	$e + O_2 \rightarrow e + O_2(A^3\Sigma_u^+, C^3\Delta_u, c^1\Sigma_u^-)$	BOLSIG+	4.5	[39,42]
R18	$e + O_2(A^3\Sigma_u^+, C^3\Delta_u, c^1\Sigma_u^-) \rightarrow e + O_2$	BOLSIG+	−4.5	[39,42]
R19	$e + O_2 \rightarrow O + O^-$	BOLSIG+	3.6	[39,42]
R20	$e + O_2 \rightarrow e + 2O$	BOLSIG+	5.58	[39,42]
R21	$e + O_2 \rightarrow e + O + O(^1D)$	BOLSIG+	8.4	[39,42]
R22	$e + O_2 \rightarrow 2e + O_2^+$	BOLSIG+	12.06	[39,42]
R23	$e + He^* \rightarrow 2e + He^+$	$1.28 \times 10^{-13} T_e^{0.6} \exp(-4.78/T_e)$	4.78	[43]
R24	$e + He_2^* \rightarrow 2e + He_2^+$	$9.75 \times 10^{-16} T_e^{0.71} \exp(-3.4/T_e)$	3.4	[43]
R25	$2He^* \rightarrow e + He + He^+$	4.5×10^{-16}	−15	[43]
R26	$e + He_2^+ \rightarrow He^* + He$	$5.0 \times 10^{-15} T_e^{-0.5}$		[44]
R27	$He^* + 2He \rightarrow He + He_2^*$	1.3×10^{-45}		[44]
R28	$He^+ + 2He \rightarrow He + He_2^+$	1.0×10^{-43}		[44]
R29	$e + He^+ \rightarrow He^*$	$6.76 \times 10^{-19} T_e^{-0.5}$		[45]
R30	$2e + He^+ \rightarrow e + He^*$	$6.186 \times 10^{-39} T_e^{-4.4}$		[45]
R31	$e + He^+ + He \rightarrow He^* + He$	$6.66 \times 10^{-42} T_e^{-2}$		[45]
R32	$2e + He_2^+ \rightarrow e + He_2^*$	1.2×10^{-33}		[45]
R33	$e + He_2^+ + He \rightarrow He^* + 2He$	3.5×10^{-39}		[45]
R34	$e + He_2^+ + He \rightarrow He_2^* + He$	1.5×10^{-39}		[45]
R35	$2e + He_2^+ \rightarrow e + He + He^*$	2.8×10^{-32}		[45]
R36	$2e + N_2^+ \rightarrow e + N_2$	$5.02 \times 10^{-39} T_e^{-4.5}$		[43]
R37	$e + N_2^+ + N_2 \rightarrow 2N_2$	$2.49 \times 10^{-41} T_e^{-1.5}$		[43]
R38	$O^- + O_2^+ \rightarrow O + O_2$	2×10^{-13}		[45]
R39	$e + 2O_2 \rightarrow O_2^- + O_2$	$5.17 \times 10^{-43} T_e^{-1}$		[31]
R40	$O_2^- + O_2^+ \rightarrow 2O_2$	2×10^{-13}		[45]
R41	$O_2^- + O_2^+ + M \rightarrow 2O_2 + M$	2×10^{-37}		[45]
R42	$He^* + N_2 \rightarrow e + N_2^+ + He$	7×10^{-17}		[31]
R43	$He_2^* + N_2 \rightarrow e + N_2^+ + 2He$	7×10^{-17}		[31]
R44	$He_2^+ + N_2 \rightarrow N_2^+ + 2He$	5×10^{-16}		[31]
R45	$He_2^+ + O_2^- \rightarrow O_2 + 2He$	1×10^{-13}		[45]
R46	$He^* + O_2 \rightarrow e + O_2^+ + He$	2.6×10^{-16}		[43]
R47	$He_2^* + O_2 \rightarrow e + O_2^+ + 2He$	3.6×10^{-16}		[43]

Note: Rate coefficients have units of $m^3 s^{-1}$ for two-body reactions and $m^6 s^{-1}$ for three-body reactions. T_e represents the electron temperature in eV. Species M in reaction R41 represents a third body. He^* represents $He(2^1S)$ and $He(2^3S)$. He_2^* represents $He_2(a^3\Sigma_u^+)$.

group, a damped Newton method with a constant damping factor is used to linearize the nonlinear equation, and the linearized equation is solved using a parallel sparse direct solver (PARDISO). The Newton iterations within the first and third groups are terminated after one iteration, while the Newton iterations within the second group are stopped at either iteration numbers of 3 or tolerance of 10^{-3}. The overall convergence criteria of the segregated iterations are satisfied when the minimum of the solution- and residual-based estimated relative errors is smaller than the specified tolerance 10^{-3}.

After the steady-state solution reaches convergence, a fully coupled solver is utilized to obtain the numerical solution of Eqs. (8)–(11) in the time-dependent calculations. The linear shape functions are applied for all dependent variables of the fully coupled system. The implicit backward differentiation formula (BDF) method, with a maximum order of five and a
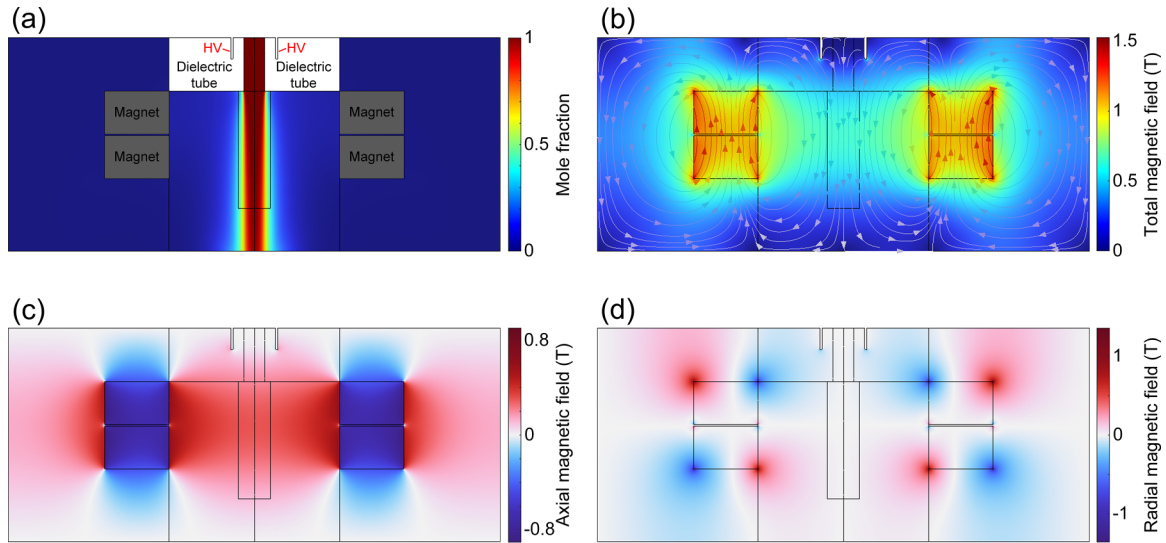
FIG. 2. The steady-state distributions of (a) He mole fraction, (b) magnetic flux density, (c) the axial component of the magnetic flux density, and (d) the radial component of the magnetic flux density.

minimum order of one, is used for time stepping. At each step, the nonlinear system is linearized by an automatic Newton iteration. PARDISO is chosen as the direct linear system solver. The time steps are automatically chosen by the BDF solver, depending on the relative and absolute tolerances that control the solution error. The maximum of the time step interval is set up to 1 ns. The absolute and relative tolerances are set to 10^{-3}. Note that the governing equations in the plasma dynamics model are solved in logarithmic form to achieve better stability.

The Debye length is expressed as $\lambda_D = 7.4 \times 10^3 \sqrt{T_e(\mathrm{eV})/n_e(\mathrm{m}^{-3})}[\mathrm{m}^{-1/2} \cdot (\mathrm{eV})^{-1/2}]$ [55]. In this paper, typical values of electron temperature and electron number density are 5 eV and 10^{18} m^{-3}, respectively. Hence, the Debye length is calculated to be 16.5 μm. To confirm our results, the grid convergence analysis is performed by mesh refinement. The refined mesh reduces the maximum mesh size to 15 μm in the region where the plasma jet flows through for the purpose of resolving the Debye length. The mesh cells and degrees of freedom are increased to 3.2×10^5 and 4×10^6. The calculations were performed on a Linux workstation equipped with Intel Xeon(R) Gold 6154 CPU @ 3.00 GHz and 3 TB RAM. The mesh refinement greatly increases the run time from 11 h to 3.3 d for a 190 ns simulation run using 72 threads. It is noted that the simulation results about the effect of the parallel magnetic field on the coaxial DBD APPJs are not influenced by the mesh refinement. The relevant data obtained before mesh refinement are selected to capture the studied physical problem on account of a small computational burden.

III. RESULTS AND DISCUSSION

A. Spatiotemporal evolutions of electron density and electric field in the parallel magnetic field

The results of steady-state neutral gas flow and magnetic field simulations are shown in Fig. 2. In the absence of a magnetic field, it is assumed that the two ring magnets are both replaced by nonmagnetic media with the same shape and size. Therefore, the calculated spatial distribution of mole fraction of species has no differences in the two cases with and without the magnetic field. The same flow field is guaranteed to exclude the possibility that the difference in the flow field leads to the difference in the subsequent discharge characteristics. In Fig. 2(a), the helium mole fraction is unity inside the tube. After the gas exits the tube, the helium mole fraction decreases in both the axial and radial directions, while the air mole fraction increases due to the convection-diffusion between helium and ambient air. The spatial distribution of the magnetic flux density in Fig. 2(b) shows that the maximum magnetic flux density on the symmetric axis is ∼0.3 T, which is quite close to the value of magnetic field employed in the experiments [16,17,27–30]. The magnetic flux density gradually increases along the radial direction in the gas discharge domain and reaches the maximum value at the position of the magnet and decreases subsequently in the region of ambient air. The streamlines and arrows in Fig. 2(b) indicate the direction of the magnetic field. In the area of streamer advancement, the magnetic field is mainly along the axial direction only with a small radial component. Therefore, the applied magnetic field is approximated as a parallel one here. The axial and radial components of the magnetic flux density are shown in Figs. 2(c) and 2(d), respectively. In these two subgraphs, red represents that a positive value for these two components, while blue represents a negative value. In the whole gas discharge domain, the axial component of the magnetic field is almost in the same direction as the gas flow. Inside the tube and near the exit ($r \leqslant 8$ mm and $z < 9$ mm), the radial component points from the outer edge of the dielectric tube to the symmetric axis, while its direction reverses at the position farther away from the tube exit ($r \leqslant 8$ mm and $z > 9$ mm). In the area of streamer development, the magnetic field in this numerical calculation presents a spatial distribution like those determined in the experiments [28,29], which facilitates the direct comparison between
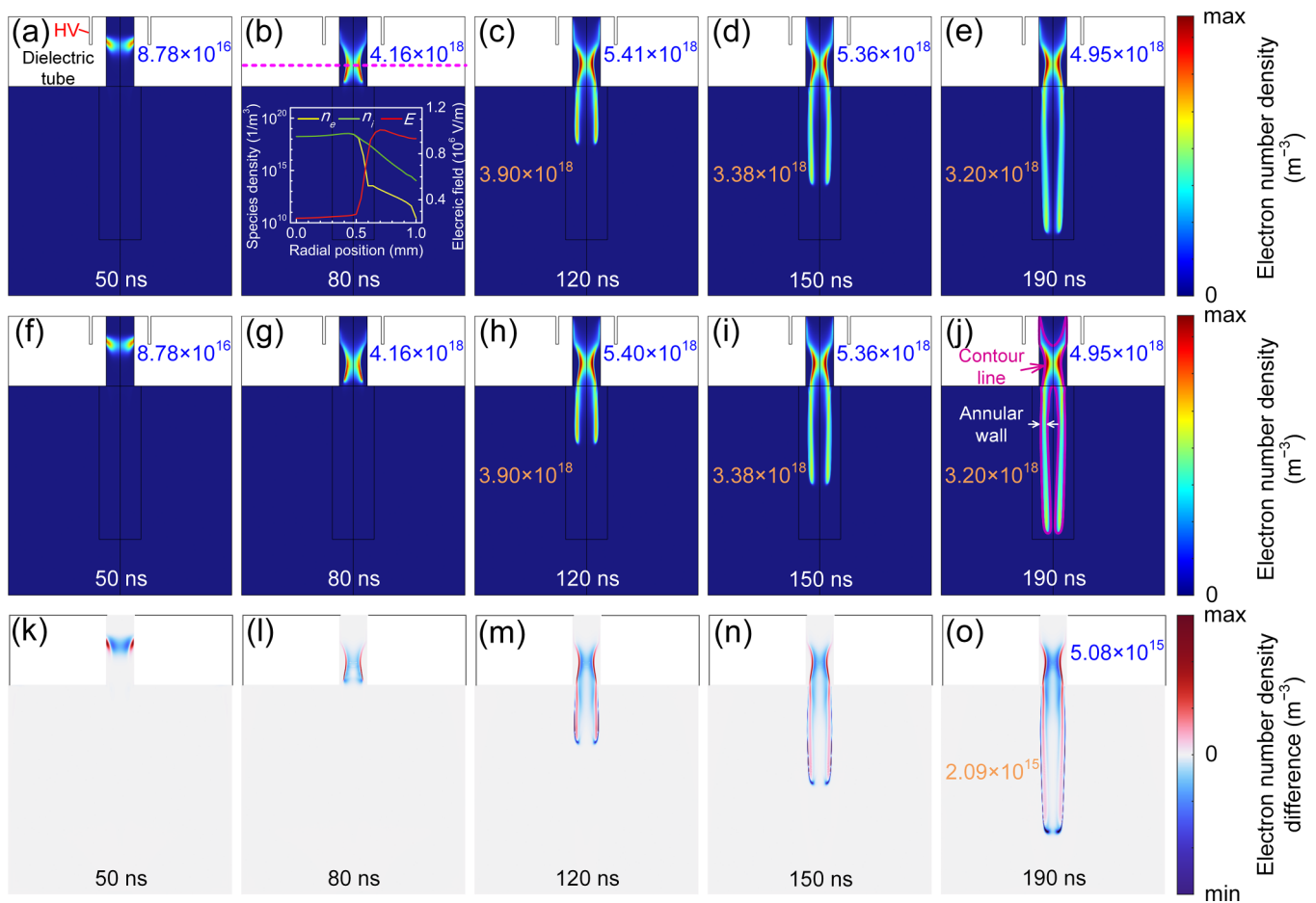
FIG. 3. The spatial distributions of electron density for the case without magnetic field at (a) 50 ns, (b) 80 ns, (c) 120 ns, (d) 150 ns, and (e) 190 ns. The spatial distributions of electron density for the case with the magnetic field at (f) 50 ns, (g) 80 ns, (h) 120 ns, (i) 150 ns, and (j) 190 ns. The spatial distributions of the difference between the electron density with the magnetic field and without magnetic field at (k) 50 ns, (l) 80 ns, (m) 120 ns, (n) 150 ns, and (o) 190 ns. The inset in (b) shows the radial distributions of electron density n_e (yellow solid line), positive ion density n_i (green solid line), and electric field E (red solid line) at the axial position of 3.5 mm (magenta dashed line) at 80 ns in the absence of magnetic field.

our theoretical simulation and the previous experimental observations [27–30].

Figures 3(a)–3(e) show the spatiotemporal evolutions of the electron density in the absence of magnetic field. The gas breakdown is triggered ~35 ns after the start of the pulse voltage with the amplitude of 3.3 kV. It follows from Fig. 3(a) that the plasma is initiated in the vicinity of the power electrode at 50 ns, and it adheres to the inner surface of dielectric tube. The streamer propagates along the direction of the gas flow. At the time of 80 ns, as shown in Fig. 3(b), the streamer head reaches the tube exit and is about to flow into the helium-air mixed layer.

The inset in Fig. 3(b) shows the radial distributions of electron density (yellow solid line), positive ion density (green solid line), and electric field (red solid line) at the axial position of 3.5 mm (magenta dashed line). At this moment, the electrical neutrality is satisfied within the range from symmetric axis to the radial position of 0.45 mm. With the increase of radial distance from the symmetric axis, the large difference of charge density accompanied by the enhanced electric field is present between the electrically neutral region and the dielectric inner surface, which is manifested as a typical

characteristic of plasma sheath. The peak electron density is located at the sheath edge, which is consistent with the α mode of a radiofrequency capacitively coupled discharge [56]. Further observation indicates that the sheath thickness initially increases and then decreases along the axial direction inside the tube.

When the jet propagates outside the tube at 120 ns [Fig. 3(c)], the discharge channel emerges as a hollow ring-shaped pattern, and the streamer head reaches the axial position of 9.1 mm. The mixed layer of helium and air is crucial for the gas discharge at this stage due to the lower ionization threshold for helium in contrast with air species. When the time increases to 150 ns [Fig. 3(d)] and 190 ns [Fig. 3(e)], a similar distribution of electron density is observed except that the plasma channel becomes longer, and the streamer head reaches the axial position of 12.0 and 15.5 mm, respectively.

The peak electron density in the dielectric tube (the blue font in Fig. 3) initially increases from 8.78×10^{16} to 5.41×10^{18} m^{-3} during the process of the streamer developing inside the tube and in the vicinity of the exit, and then gradually decreases to 4.95×10^{18} m^{-3} as the streamer further proceeds

forward. For the maximum electron density outside the dielectric tube (the orange font in Fig. 3), it rises from 2.38×10^{18} m^{-3} at 90 ns (not shown in this paper) to 3.90×10^{18} m^{-3} at 120 ns and then falls to 3.20×10^{18} m^{-3} at 190 ns. The peak electron densities both inside and outside the tube first increase and then decrease. This phenomenon was also reported by other groups [31,57].

Figures 3(f)–3(j) show the spatiotemporal evolutions of the electron density in the presence of magnetic field. Compared with the case without a magnetic field at the same moment, there is no significant variation in the evolution of the electron density. This means that the parallel magnetic field almost has no effect on the streamer propagation and contributes little to length variation of the coaxial DBD plasma jet, which agrees well with the experimental observations [27,28]. The magenta curve in Fig. 3(j) is the contour line with the electron density of 1.18×10^{18} m^{-3} (equal to 1/e of the maximum electron density outside the tube at 190 ns). It needs to be noted that only the line segments outside the tube are defined as the boundary for the annular wall. Most of the charged particles of the plasma jet are concentrated in the annular wall, and the charge density rapidly decreases along the direction away from the annular wall.

To conduct a more detailed analysis of the effect of a magnetic field on a plasma jet, the electron density without the magnetic field is subtracted from the electron density with the magnetic field, as shown in Figs. 3(k)–3(o). In the color bar on the right side of these subgraphs, red represents a higher electron density with the magnetic field than that without the magnetic field, while blue represents a lower electron density with the magnetic field than that without the magnetic field. As shown in Fig. 3(o), the maximum difference values inside and outside the tube are 5.08×10^{15} and 2.09×10^{15} m^{-3}, respectively. They only account for 0.10% of the maximum value of 4.95×10^{18} m^{-3} inside the tube and for 0.07% of the maximum value of 3.20×10^{18} m^{-3} outside the tube. It is concluded that the sheath thickness inside the dielectric tube in the presence of the magnetic field is slightly thinner than that in the absence of the magnetic field. After the streamer propagates outside the dielectric tube, the electrons exhibit a little more concentrated distribution in the annular wall in the presence of the magnetic field. The jet length in the presence of the magnetic field is slightly shorter than that in the absence of the magnetic field.

Figures 4(a)–4(e) show the spatial distributions of electric field with the applied magnetic field at 50, 90, 120, 150, and 190 ns, respectively. At 50 ns, the electric field is approximately distributed uniformly in the discharge space of interest inside and outside the tube in Fig. 4(a). When it comes to 90 ns in Fig. 4(b), the discharge space is somewhat disturbed, and a high electric field is observed very close to the inner tube surface approaching the exit. In addition, at this moment, the streamer develops out of the tube, and there also exists a relatively high electric field both around the plasma channel and in front of the streamer head. At 120, 150, and 190 ns, a similar distribution of electric field is presented, as shown in Figs. 4(c)–4(e), except that this high electric field extends along the gas flow.

The axial profiles of the electric field at $r = 0$ mm (symmetric axis) and $r = 0.7$ mm in the presence of magnetic field are both plotted at the time of interest [90 ns (magenta lines),120 ns (blue lines), 150 ns (green lines), and 190 ns (red lines)], as shown in Fig. 4(f). The electric field first increases and then decreases with increasing the axial position at the four moments of interest, whether the radial position is 0 or 0.7 mm. This profile indicates that the electric field in the streamer head is much higher than that behind the streamer head. On the symmetric axis (dashed lines), the maximum values of the electric field are 1.00×10^{6}, 9.31×10^{5}, 9.59×10^{5}, and 1.07×10^{6} V m^{-1}, respectively, obtained at 90, 120, 150, and 190 ns. When it comes to the radial position 0.7 mm away from the symmetric axis (solid lines), the maximum electric field is increased compared with that on the symmetric axis at the same moment. The maximum electric field at the radial position of 0.7 mm first rises from 1.36×10^{6} V m^{-1} at 90 ns to 1.57×10^{6} V m^{-1} at 120 ns and then falls to 1.55×10^{6} V m^{-1} at 150 ns and 1.42×10^{6} V m^{-1} at 190 ns. Our further simulation indicates that the axial profiles of the electric field at the same moment and the same radial position in the absence of the magnetic field (not presented here) are like those in the presence of the magnetic field in Fig. 4(f). The maximum electric field at the radial position of 0.7 mm also increases first and then decreases during the process of the streamer developing outside the tube.

B. Spatiotemporal evolutions of electron energy, Hall parameter, and $E \times B$ field in the parallel magnetic field

The spatial distributions of electron energy for the case with the magnetic field at 50, 80, 120, 150, and 190 ns are respectively shown in Figs. 5(a)–5(e). At 50 ns, the peak electron energy of 7.0 eV is obtained near the inner dielectric surface at the downstream of the power electrode. The electron energy gradually decreases toward both ends of the tube on the whole, as shown in Fig. 5(a). The maximum electron energy outside the tube of 5.6 eV is located at the vicinity of the tube exit. When the streamer head approaches the tube exit at 80 ns in Fig. 5(b), a high electron energy is observed in the region between the plasma channel and the inner dielectric wall where the plasma sheath locates as well as the streamer head in the front of the plasma channel. The peak electron energy of 9.2 eV within the investigated domain appears in the plasma sheath on the side near the edge of plasma channel in the vicinity of tube exit. The maximum electron energy outside the tube is increased to 7.9 eV. After the plasma jet propagates outside the tube, the high electron energy still exists in the plasma sheath and the streamer head. Moreover, the electron energy surrounding the lateral surface of plasma channel is ~50% lower than that at the streamer head. At 120 ns in Fig. 5(c), the peak electron energy is 9.3 eV in the plasma sheath inside the tube. The maximum electron energy outside the tube (8.3 eV) is located off axis at the streamer head, and the electron energy surrounding the lateral surface of plasma channel is ~4–5 eV. When it comes to 150 and 190 ns, a similar spatial distribution of electron energy is presented, respectively, in Figs. 5(d) and 5(e), except for its extension along with the streamer advancement. The maximum electron energy in the plasma sheath inside the tube falls to 8.5 eV at 150 ns and 7.4 eV at 190 ns. The maximum
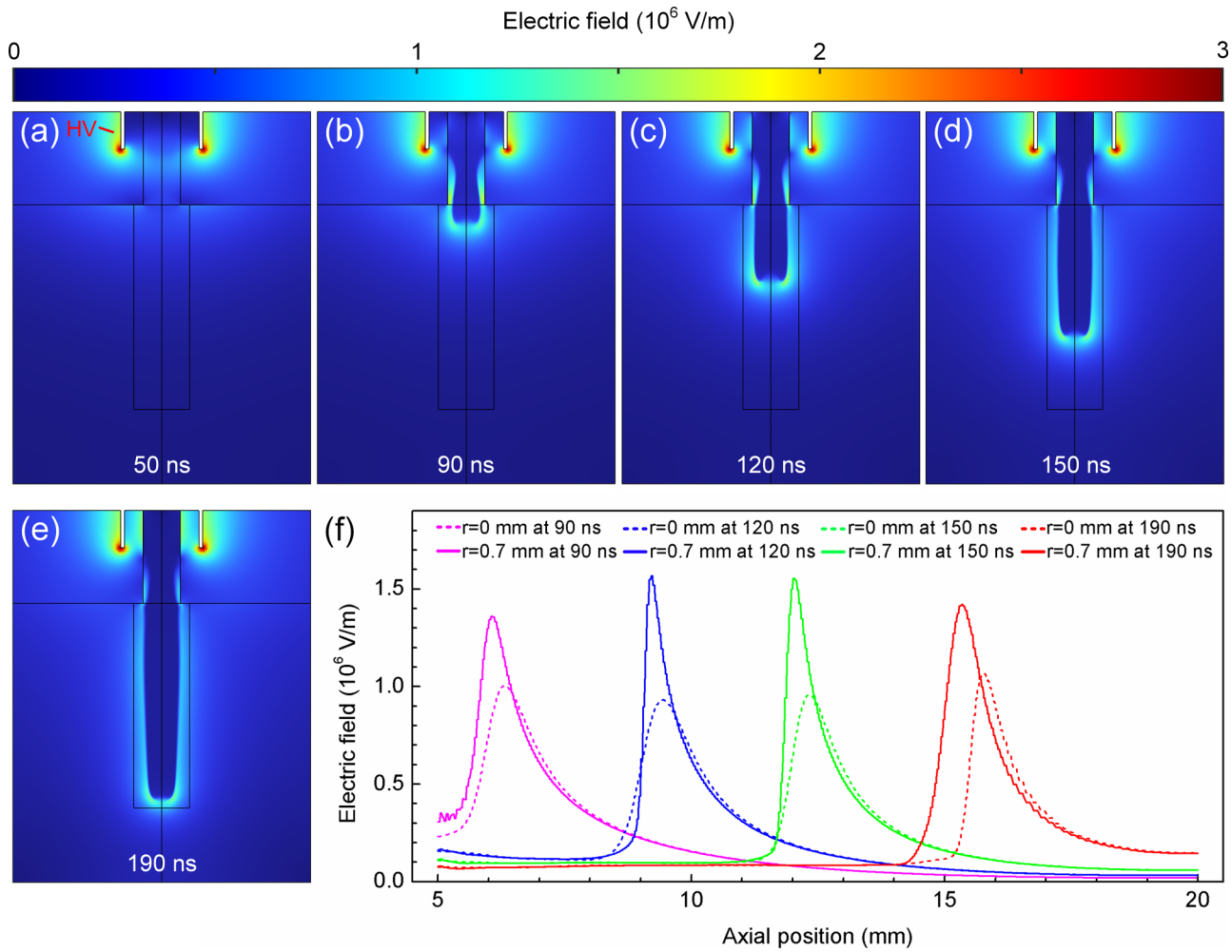
FIG. 4. The spatial distributions of electric field for the case with the magnetic field at (a) 50 ns, (b) 90 ns, (c) 120 ns, (d) 150 ns, and (e) 190 ns. (f) The axial distributions of electric field on the symmetric axis (dashed lines) and at the radial position of 0.7 mm (solid lines) for the case with the magnetic field at 90 ns (magenta lines), 120 ns (blue lines), 150 ns (green lines), and 190 ns (red lines).

electron energy at the streamer head decreases to 8.1 eV at 150 ns and 8.0 eV at 190 ns.

Figures 5(f)–5(j) show the spatial distributions of total electron collision frequency in the presence of the magnetic field at 50, 80, 120, 150, and 190 ns, respectively. The spatial distributions of Hall parameter at the corresponding moments are plotted in Figs. 5(k)–5(o). As shown in Fig. 5(f), the spatial distribution of the total electron collision frequency is like that of the electron energy at 50 ns in Fig. 5(a). The peak value of the total electron collision frequency (2.2×10^{12} Hz) is also obtained near the inner dielectric surface at the downstream of the power electrode inside the tube. The Hall parameter is very small in the regions with higher electron energy and electron collision frequency, as shown in Fig. 5(k). Especially at the position where the plasma locates, the Hall parameter is only $\sim$0.003, which is $\ll$1. The Hall parameter is significantly increased ($\gg$1) in the area further away from the tube exit and closer to the two permanent ring magnets, as a result of the increased magnetic field.

Until 80 ns, in view of the fact that the streamer discharge takes place inside the tube, the spatial distributions of the total

electron collision frequency [Fig. 5(g)] and Hall parameter [Fig. 5(l)] basically remain unchanged outside the tube. Inside the tube, the total electron collision frequency in the plasma sheath is higher than that in the plasma channel. The peak value of the total electron collision frequency (2.4×10^{12} Hz) is also acquired in the plasma sheath on the side near the edge of plasma channel in the vicinity of tube exit, which is consistent with that of the electron energy in Fig. 5(b). The Hall parameter in the plasma channel where the electrons are concentrated ($\sim$0.01–0.02) is slightly larger than that in plasma sheath ($\sim$0.01).

After the plasma jet is ejected from the tube, the total electron collision frequency surrounding the lateral surface of plasma channel is larger than that in the plasma channel, as shown in Figs. 5(h)–5(j). Moreover, a higher total electron collision frequency can also be observed at the streamer head in the front of the plasma channel and in the plasma sheath inside the tube. At 120 ns in Fig. 5(m), the Hall parameter in the annular wall reaches its maximum value ($\sim$0.07) near/on the lateral surface of the plasma channel, from which it decreases along the direction of the negative *r* axis. It is
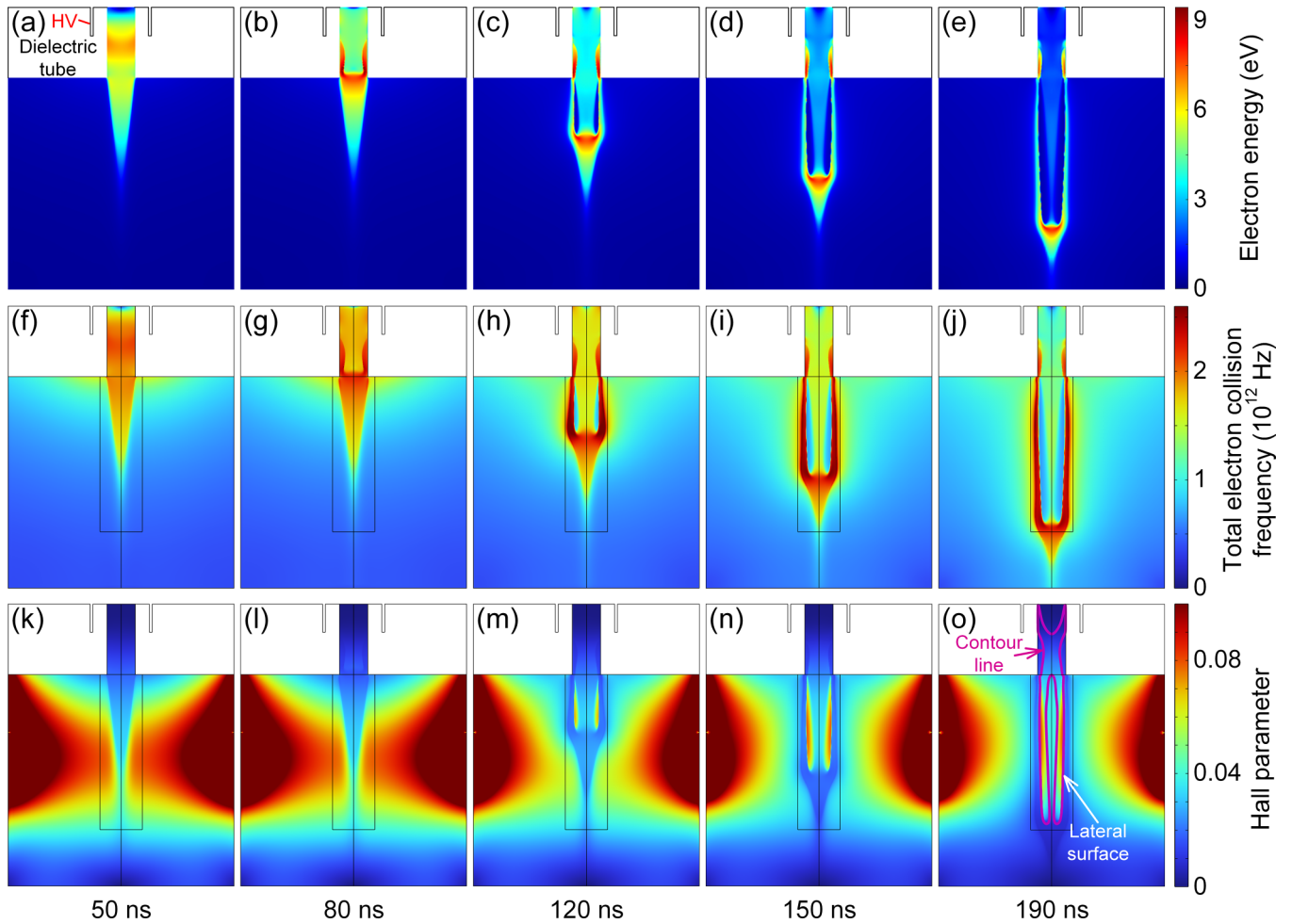
FIG. 5. The spatial distributions of electron energy for the case with the magnetic field at (a) 50 ns, (b) 80 ns, (c) 120 ns, (d) 150 ns, and (e) 190 ns. The spatial distributions of total electron collision frequency for the case with the magnetic field at (f) 50 ns, (g) 80 ns, (h) 120 ns, (i) 150 ns, and (j) 190 ns. The spatial distributions of Hall parameter for the case with the magnetic field at (k) 50 ns, (l) 80 ns, (m) 120 ns, (n) 150 ns, and (o) 190 ns.

only ~0.02 in the region surrounding the lateral surface of the plasma channel and in the streamer head where the higher electron energy and higher total electron collision frequency are observed.

With increasing the time to 150 and 190 ns, a similar spatial distribution of the Hall parameter is acquired, respectively, in Figs. 5(n) and 5(o), except that the red area in the plasma channel extends to a longer distance, and the blue area around the plasma channel expands in the investigated domain. The Hall parameter in the annular wall reaches its maximum values of 0.080 at 150 ns and 0.083 at 190 ns near/on the lateral surface of the plasma channel. It is larger in the middle part of the annular wall along the axial direction. The Hall parameter in the region surrounding the lateral surface of the plasma channel and in the streamer head still maintains at 0.02 or so at 150 and 190 ns.

The spatial distribution of the Hall parameter can be understood based on the orientation of the electric field with respect to the magnetic field. In the streamer head, the electric field is nearly parallel to the magnetic field, where the electron energy and electron collision frequency are relatively high. The mobility along the electric field direction changes quite little.

Hence, the Hall parameter in the streamer head is relatively small. Near/on the lateral surface of the plasma channel, the electric field is nearly perpendicular to the magnetic field, and the electron energy and electron collision frequency are relatively small. The mobility along the electric field direction is reduced to some extent. Therefore, the Hall parameter reaches a relatively higher value here. In the region surrounding the lateral surface of the plasma channel, the electric field is still perpendicular to the magnetic field, but the electron energy and electron collision frequency are increased compared with those on the lateral surface of plasma channel. As a result, the Hall parameter is decreased compared with that on the lateral surface of plasma channel. In the annular wall, although the electron energy and electron collision frequency are reduced compared with those on the lateral surface of plasma channel, the Hall parameter is moderately decreased compared with that on the lateral surface of plasma channel. This is because the electric field is almost parallel to the magnetic field.

As we know, the plasma sheath is a positive space-charge region shielding the neutral plasma from the dielectric wall or metal electrode [58]. Because of the higher mobility of electrons than that of ions, the electrons are absorbed to the

part of the inner surface of the tube that is parallel to the power electrode. The repulsion of the accumulated electrons on the inner surface against the electrons inside the tube prevents them from migrating to the vicinity of the tube wall. Therefore, a large charge density difference between positive ions and electrons is formed in the sheath. The magnetic field inside the tube is mainly along the axial direction, as shown in Fig. 2(b). According to Eqs. (18) and (19), the decrease of electron mobility radially reduces the number of electrons accumulated on the dielectric wall. Consequently, the repulsive effect weakens, and a thinner sheath is acquired in the presence of the magnetic field. In our case, the Hall parameter inside the tube is ∼0.01–0.02 as mentioned above, which means a tiny reduction both in electron mobility and the ultimate sheath thickness.

In the annular wall, the Hall parameter reaches ∼0.08 near/on the lateral surface of the plasma channel, and the radial diffusion coefficients of electrons and ions with the applied magnetic field are accordingly decreased to 0.9936 of that without the magnetic field. The small decrease of the coefficient hinders the inward and outward radial diffusions of charged particles in the annular wall to some degree. On the other hand, a confinement effect is imposed on the high-energy electrons in the avalanche heads by the Lorentz force during the process of streamer evolution [20–22]. The radial expansion of the wedge-shaped avalanche heads is thus restricted with the applied magnetic field. These two factors are probably responsible for the little more concentrated electron distribution in the annular wall under the effect of the magnetic field.

Also, the Hall parameter in the streamer head maintains at 0.02 or so, which means the propagation of the ionization wave along the axial direction is hindered at a very least level. Therefore, it is reasonable that the length of the plasma jet is reduced after applying the parallel magnetic field. The shortened jet length in the presence of the parallel magnetic field is further elaborated as below.

From the perspective of the particle orbit theory, the $E \times B$ drift of the charged particles is suitable for elucidating the reduced jet length in the presence of the magnetic field [59]. In our case, $E \times B = (E_z B_r - E_r B_z)e_\theta$, where E_z and E_r correspond to the axial component and radial component of the electric field, B_r and B_z correspond to the radial component and axial component of the magnetic field, and e_θ is the unit vector of the θ axis. The spatial distributions of the $E \times B$ field at the time of interest (50, 80, 90, 120, 150, and 190 ns) are calculated and plotted in Fig. 6. In these subgraphs, the red represents that the direction of the $E \times B$ field is along the positive θ axis (clockwise looking in the direction of the streamer advancement), while the blue represents that the direction of the $E \times B$ field is along the negative θ axis (counterclockwise looking in the direction of the streamer advancement).

It is found that a line [magenta dashed curve shown in Fig. 6(a)], which divides the entire discharge space into two parts, is present at 50 ns. In the region above the dividing line with a smaller z value (except for the sharp corner of the tube exit), the $E \times B$ field is along the negative θ axis. The $E \times B$ field is along the positive θ axis in the region below the dividing line with a larger z value. Due to a large electric field
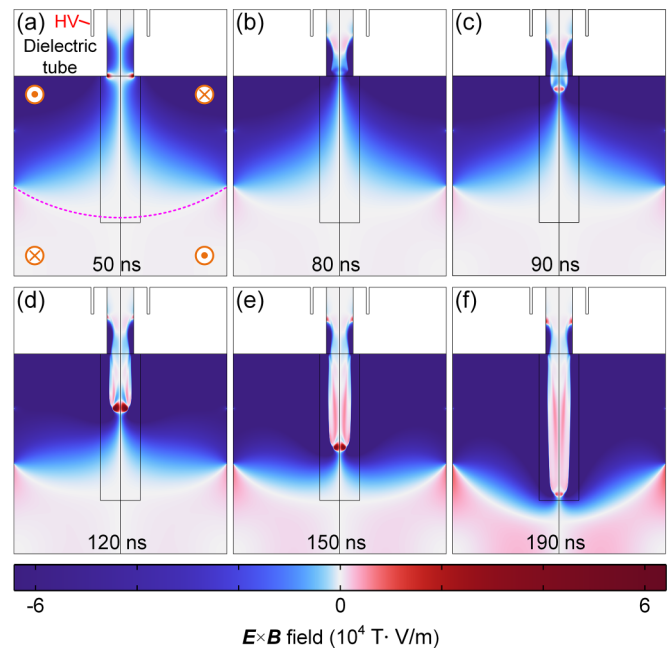

FIG. 6. The spatial distributions of $E \times B$ field for the case with the magnetic field at (a) 50 ns, (b) 80 ns, (c) 90 ns, (d) 120 ns, (e) 150 ns, and (f) 190 ns.

along the negative r axis at the sharp corner of the tube exit at 50 ns, the $E \times B$ field here is along the positive θ axis, which is distinct from other nearby locations. As shown in Fig. 6(b), when it is 80 ns, this dividing line still exists, and its position remains almost unchanged. Because of the spatial distribution of the electric field inside the tube being disturbed by the streamer discharge, the $E \times B$ field in the plasma channel closer to the power electrode, as well as that at the sharp corner of the tube exit, is changed to the opposite direction of that at 50 ns. As the plasma jet propagates forward, the streamer discharge continues to disturb the spatial distribution of electric field outside the tube, and the direction of the $E \times B$ field at the on-axis front end of the plasma channel is altered to the positive θ axis at 90 ns in Fig. 6(c). When it comes to 120 ns, in addition to the on-axis front end of the plasma channel, the $E \times B$ field in the annular wall outside the tube also presents a positive θ-axis direction, as indicated by the red area in Fig. 6(d). With the time increased to 150 ns in Fig. 6(e) and 190 ns in Fig. 6(f), this red area extends with the increase of the plasma jet length. It is revealed that the $E \times B$ field is mainly along the positive θ axis in the plasma channel, where electrons and ions are mainly distributed. The particle orbit theory shows that the $E \times B$ field makes the electrons and ions drift in the azimuthal direction in the presence of the magnetic field, which is deviated from their original axial-direction trajectories dominated by the electric field, and therefore, the development of the plasma jet is hindered in the axial direction. Namely, the $E \times B$ drift is responsible for the tiny reduction in the length of the plasma jet with the application of the magnetic field.

Above all, the parallel magnetic field has a minor impact on the APPJs generated with the coaxial DBD. The tiny reduction of sheath thickness inside the tube is attributed to the

reduced number of accumulated electrons on the dielectric inner surface. The little more concentrated electron distribution in the annular wall outside the tube is ascribed to the decreased electron diffusion in the radial direction and the confinement effect of parallel magnetic field on the electrons in the avalanche heads. The slightly shortened jet length is induced by the $\boldsymbol{E} \times \boldsymbol{B}$ drift of electrons and ions. Our simulation results are quite different from the experimental observations in the parallel-plate DBD, where a notable impact of the parallel magnetic field on the plasma generation was observed.

C. Comparative analysis of the coaxial DBD and parallel-plate DBD in the parallel magnetic field

As aforementioned, the discharge improvement in the parallel-plate DBD is caused by the enhancement of the memory effect and the confinement of the magnetic field on electrons [20–22]. Firstly, the discharge occurs three times in sequence within one voltage pulse for the parallel-plate DBD with the gas gap of several millimeters. After the primary discharge, the residual charges (basically the ions) in the microdischarge channel facilitate the formation of the secondary and tertiary discharges in the same spot. The enhanced primary discharge generated more residual charges with the parallel magnetic field, which lead to a prominent increase in the intensity of the tertiary discharge. However, for the free-expanding coaxial DBD APPJs excited by pulsed-DC power in our case, only one discharge pulse is considered for most of the experimental situations [27,28], and there is no chance for the residual charges to promote the secondary and tertiary discharges in the same discharge phase. That is to say the memory effect almost contributes nothing to the improvement of free-expanding coaxial DBD APPJs.

Secondly, in the DBD with parallel-plate configuration, the moving direction of the surface electrons under the electrostatic repulsion is perpendicular to the direction of the magnetic field. The Lorentz force imposed on the surface electrons is considerably large. The lateral expanding of surface electrons is reduced with the confinement of the parallel magnetic field, which decreases the decay of the surface electrons. Thus, the number of surface electrons is increased, and the discharge is enhanced [20]. Nevertheless, in the coaxial DBD with parallel magnetic field applied, the moving direction of the surface electrons under the electrostatic repulsion is parallel to the direction of the magnetic field. The confinement effect of the magnetic field on the surface electrons is extremely weak due to the small radial component of the magnetic field in our case. Instead, the confinement of the parallel magnetic field on the free electrons in the discharge space prevent some electrons from drifting to the tube surface. As a result, the number of surface electrons is reduced, and the enhancement of discharge due to the confinement of the magnetic field on electrons is not obtained.

D. Spatial distributions of typical species in the parallel magnetic field

Since various positive ions, including He^+, He_2^+, N_2^+, and O_2^+, are produced in the discharge, it is necessary to analyze the spatial distributions of these species in the plasma jet. Here, the spatial distributions of O and $O(^1D)$ are also discussed due to their high oxidative stress. Figure 7 shows the spatial distribution of species density in the presence of the magnetic field at 190 ns. The species density in the absence of the magnetic field at the same moment has an analogous spatial distribution with that in the presence of the magnetic field and thus is not presented here. For the helium species in Figs. 7(a) and 7(d), He^+ and He_2^+ are concentrated in the streamer head and in the plasma channel inside the tube, respectively. The peak value of N_2^+ in Fig. 7(b) is higher than that of He^+ in the streamer head. In Fig. 7(e), O_2^+ has the same distribution profile as N_2^+, and the slight difference is that most of them are confined in the region closer to the outlet of the tube. These results indicate that the electron impact ionization of helium and nitrogen atoms (R3 and R10 in Table IV) is the major ionization reaction in the streamer head, and Penning ionization (R42, R43, R46, and R47 in Table IV) is the dominant contributor to the ionization along the channel behind the streamer head [33]. The distribution of O in Fig. 7(c) and $O(^1D)$ in Fig. 7(f) in the annular wall is more uniform than the other species, and their peak values are even higher than that of N_2^+ and O_2^+, which is the key source of the reactivity of the plasma jet. Considering the close correlation between the optical emission and the active species, the similar spatial distributions and nearly identical density values of the species in the two cases indicate that the parallel magnetic field has little impact on the luminous intensity of plasma jet, which is consistent with the previous experiment results [27,28].

To explicitly elucidate the impact of the magnetic field on these positive ions and active species, the species density without the magnetic field is subtracted from the species density with the magnetic field, and its difference is plotted in Fig. 8 in the same way as the electron density aforementioned. As shown in Fig. 8(a), the He^+ density is increased along the channel behind the streamer head but decreased in the streamer head with the magnetic field applied. The He_2^+ ion density inside the tube gets higher at the radial position farther away from the symmetric axis in the presence of the magnetic field in Fig. 8(d). It agrees with the previous observation that the magnetic field decreases the sheath layer thickness. Due to the fact that He_2^+ accounts for the majority of positive ions in the plasma channel inside the tube and the plasma channel presents the electrically neutral characteristics, the variation of the spatial distribution of He_2^+ ions in the presence of the magnetic field is like that of electrons inside the tube. The ion densities for N_2^+ in Fig. 8(b) and O_2^+ in Fig. 8(e) represent a more concentrated distribution in the annular wall under the effect of the magnetic field. This is consistent with the previous observation from the electron density distribution, as indicated in Figs. 3(k)–3(o). However, it follows that the spatial distribution of O and $O(^1D)$ contracts radially in the presence of magnetic field, respectively, shown in Figs. 8(c) and 8(f). The effect of magnetic field on O and $O(^1D)$ is little different from that on N_2^+ and O_2^+, which may be caused by the different reaction pathways and distinct reaction competition modes in production and consumption of these species, as listed in Table IV.
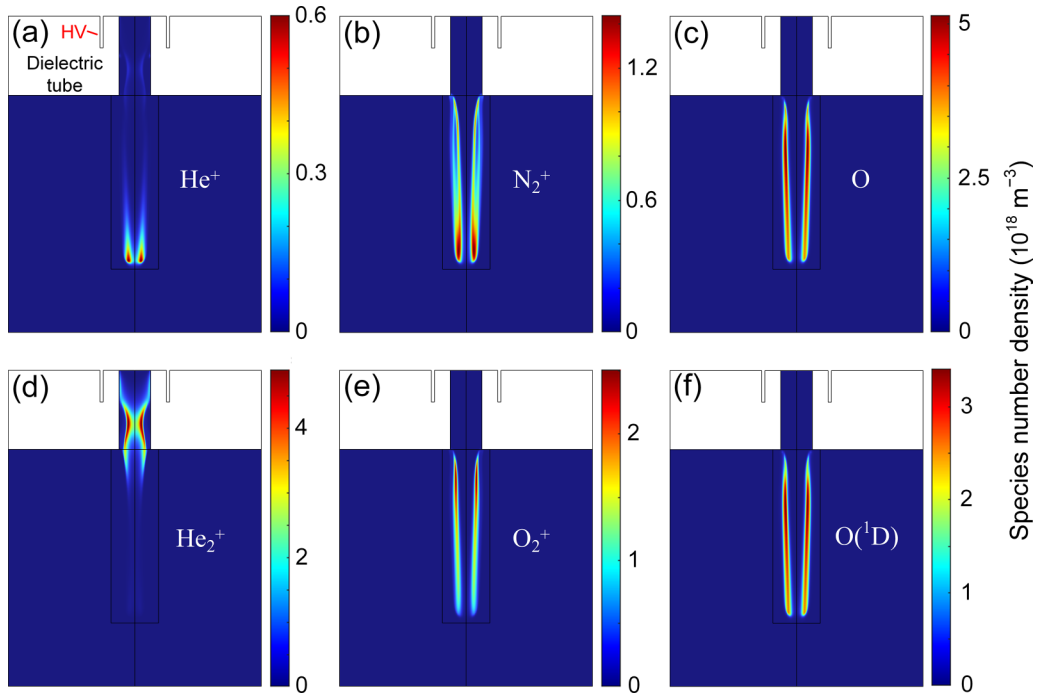
FIG. 7. The spatial distributions of the species density for the case with the magnetic field at 190 ns: (a) He$^+$, (b) N$_2^+$, (c) O, (d) He$_2^+$, (e) O$_2^+$, and (f) O(^{1}D).

E. Spatiotemporal evolutions of the ionization rate and streamer propagation in the parallel magnetic field

To delve into the propagation dynamics of the plasma jet, the total ionization rate (including ionization of He, N$_2$, and O$_2$) of the plasma jet at the four moments of interest (90, 120, 150, and 190 ns) in the absence of the magnetic field is shown in Fig. 9(a). The total ionization rate is mostly concentrated in the streamer head with less ionization distributed along the
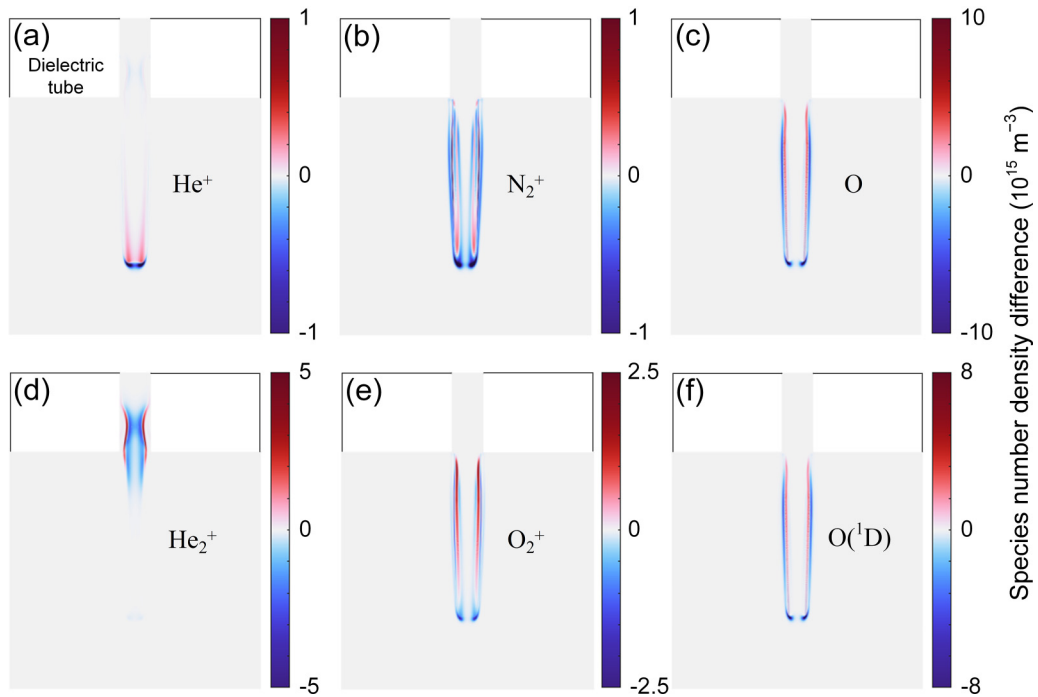

FIG. 8. The spatial distributions of the difference between the species density with the magnetic field and without magnetic field at 190 ns: (a) He$^+$, (b) N$_2^+$, (c) O, (d) He$_2^+$, (e) O$_2^+$, and (f) O(^{1}D).
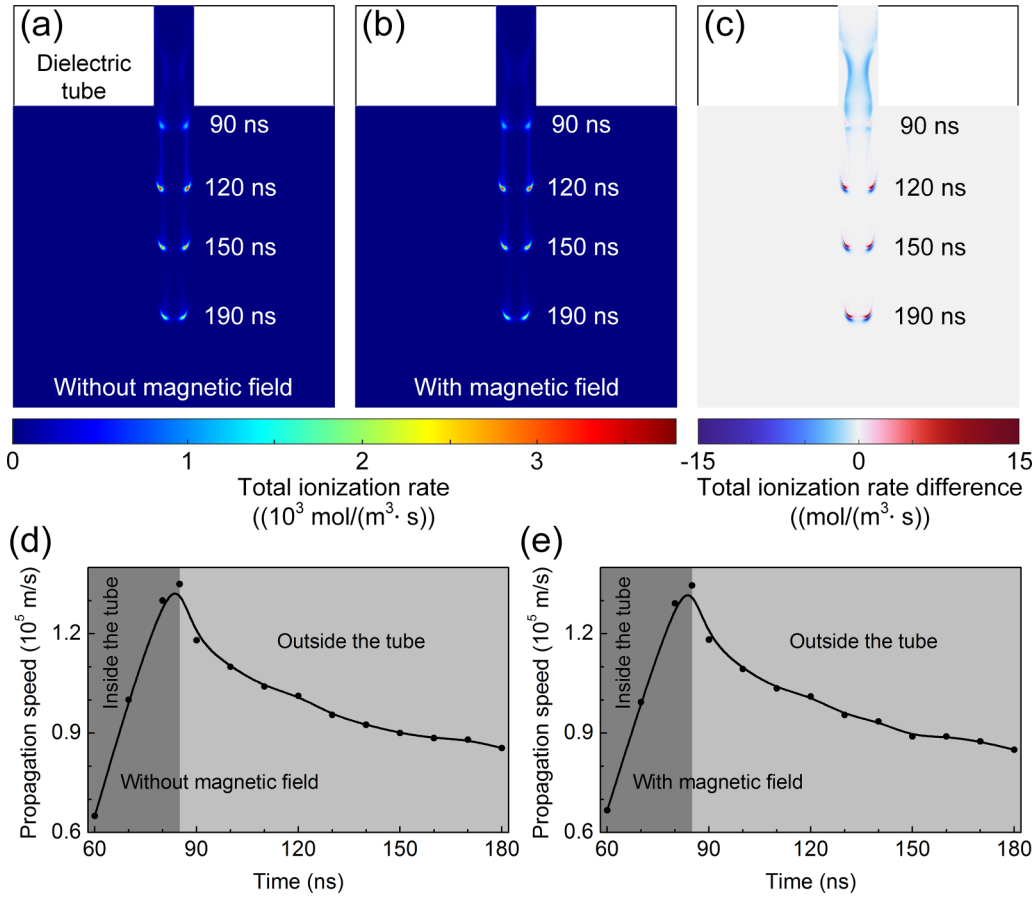
FIG. 9. The total ionization reaction rates at 90, 120, 150, and 190 ns for the case (a) without magnetic field and (b) with the magnetic field. (c) The differences between the total ionization reaction rates with the magnetic field and without magnetic field at 90, 120, 150, and 190 ns. And the temporal evolutions of the streamer propagation speed for the case (d) without magnetic field and (e) with the magnetic field.

channel behind the streamer head. The peak ionization was located off axis in the streamer head, which is the same as the plasma bullet with a ring structure captured by the ICCD image in the experiment [25]. It is generally recognized that the ionization wave will propagate along the He-air mixed layer where the He concentration is ∼99%, which is in favor of promoting the ionization processes [57]. According to the mole fraction profile in Fig. 2(a), it is reasonable that the radial position of the peak value of the total ionization rate gradually approaches the symmetry axis with increasing the propagation distance of the ionization wave. The peak ionization rate first increases from 1200 mol/(m^3 s) at 90 ns to 3789 mol/(m^3 s) at 120 ns and then decreases to 2925 mol/(m^3 s) at 150 ns and 2253 mol/(m^3 s) at 190 ns. Figure 9(b) shows the total ionization rates at the same four moments in the presence of the magnetic field. It is found that the spatial distribution and peak value of the total ionization rate have no significant difference from that in Fig. 9(a) at the same moment. The total ionization rate in the two cases with and without the magnetic field spatiotemporally evolves in the similar manner. During the process of the streamer developing outside the tube, the initial increase and subsequent decrease of peak ionization rate may be caused by the temporal evolution of maximum electric field at the radial position of 0.7 mm, as described in Fig. 4. To compare the streamer head with and without the magnetic field at the same time, the total ionization rate

without the magnetic field is subtracted from that with the magnetic field, with the results shown in Fig. 9(c). It is found that the propagation distance of the streamer head at the same time is slightly shorter in the presence of the magnetic field. This agrees well with the minor reduction in the jet length aforementioned.

The streamer propagation speed is calculated according to the axial position of the peak ionization rate. The temporal evolutions of the streamer propagation speed for the case without and with the magnetic field are plotted, respectively, in Figs. 9(d) and 9(e). The applied magnetic field has little impact on the streamer dynamics. In the initial stage of streamer development, the propagation speed rapidly increases inside the dielectric tube. The maximum propagation speed of 1.35×10^5 m/s is obtained when the streamer head reaches the proximity of the tube exit at 85 ns. After that, the streamer advances forward with a gradually decreasing speed outside the tube. It should be noted that the same or similar spatiotemporal evolution of the streamer propagation was observed in the previous experiment [60]. The initial increase of the propagation speed inside the tube is due to the rapid deposition of discharge energy into the gas during the current pulse that is initiated at the rising edge of the applied voltage [61]. When the streamer propagates outside the tube, with increasing the axial position, the energy coupled from the decreasing applied electric field [Fig. 1(c)]

to the streamer declines, and the energy consumed by the increasing air mole fraction [Fig. 2(a)] grows [60]. Therefore, the streamer gradually decelerates until it disappears in the end.

IV. CONCLUSIONS

Based on the two-dimensional axisymmetric fluid model, a numerical simulation was carried out to investigate the influence of an applied parallel magnetic field on the coaxial DBD plasma jet driven by pulsed-DC voltage at atmospheric pressure. The parallel magnetic field ($\sim$0.3 T on the symmetric axis) was obtained by stacking two ring magnets downstream the outer side of the dielectric tube.

The microscopic variations of the atmospheric plasma jet after applying the parallel magnetic field observed from the spatiotemporal evolution of electron density are qualitatively and quantitatively elucidated based on the spatiotemporal evolutions of Hall parameter and $E \times B$ field. A slightly thinner sheath inside the tube is present in the presence of the parallel magnetic field as a result of the decreased accumulated electrons on the inner surface of dielectric tube. After the streamer propagates outside the tube, a little more concentrated electron distribution in the annular wall is observed with the application of the parallel magnetic field because of the reduced electron diffusion in the radial direction and the confinement effect of the magnetic field on the electrons in the avalanche heads. The $E \times B$ drift of charged particles is the main cause of the tiny reduction in the jet length with the applied magnetic field.

A strong electric field is induced in the plasma sheath inside the tube, where the electron energy and the electron collision frequency are both high. The electric field, electron energy, and electron collision frequency in the streamer head and in the region surrounding the lateral surface of plasma channel are much higher than those along the plasma channel behind the streamer head. The spatial distribution of typical positive ions indicates that the electron impact ionization of helium and nitrogen atoms is the major ionization reaction in the streamer head, and Penning ionization dominates along the channel behind the streamer head. The parallel magnetic field hardly affects the spatial distribution of the positive ions and active species.

The peak ionization rate is first increased and then decreased outside the tube, which is originated from the temporal evolution of the off-axis maximum electric field

in the streamer head. The streamer first accelerates inside the tube, reaching its maximum speed near the tube exit, and then gradually decelerates. The initial acceleration is due to the rapid deposition of discharge energy into the gas during the current pulse that is initiated at the rising edge of the applied voltage. The subsequent deceleration is attributed to the reduced energy coupling from the weaker applied electric field to the streamer and the increased energy consumption by the higher air mole fraction. The streamer propagation speed is not impacted by the parallel magnetic field.

These results demonstrate that the parallel magnetic field has no apparent effect on the dynamics behavior of the plasma jet and contributes little to the performance improvement of coaxial DBD. The reason for this little impact of the parallel magnetic field on coaxial DBD is further clarified by comparing with the case of parallel-plate DBD. On the one hand, the memory effect almost contributes nothing to the improvement of the free-expanding coaxial DBD plasma jet, when only one discharge pulse occurs. On the other hand, the confinement of the magnetic field on surface electrons is weak because the moving direction of the surface electrons under the electrostatic repulsion is parallel to the magnetic field lines. The number of surface electrons is reduced with the parallel magnetic field preventing the free electrons in the discharge space from drifting to the tube surface.

These simulation results offer insight into the effect of magnetic field on plasma jets, but more experiments and simulations are still needed to further clarify the enhancement effect of the parallel magnetic field on the coaxial DBD plasma jets. The microscopic variations of the plasma jet observed in the simulation could be validated experimentally with the development of plasma diagnostics techniques in the future. Additionally, instead of the drift-diffusion theory, other numerical simulation models, including the Monte Carlo method, could be used to predict some details of the streamer discharge in the presence of the parallel magnetic field.

ACKNOWLEDGMENTS

---

[1] M. Laroussi and T. Akan, Arc-free atmospheric pressure cold plasma jets: A review, Plasma Process. Polym. **4**, 777 (2007).

[2] A. Shashurin, M. Keidar, S. Bronnikov, R. A. Jurjus, and M. A. Stepp, Living tissue under treatment of cold plasma atmospheric jet, Appl. Phys. Lett. **93**, 181501 (2008).

[3] A. J. Knoll, P. Luan, E. A. J. Bartis, C. Hart, Y. Raitses, and G. S. Oehrlein, Real time characterization of polymer surface modifications by an atmospheric-pressure plasma jet: Electrically coupled versus remote mode, Appl. Phys. Lett. **105**, 171601 (2014).

[4] T. Abuzairi, M. Okada, S. Bhattacharjee, and M. Nagatsu, Surface conductivity dependent dynamic behaviour of an ultrafine atmospheric pressure plasma jet for microscale surface processing, Appl. Surf. Sci. **390**, 489 (2016).

[5] F.-H. Kuok, C.-Y. Liao, T.-H. Wan, P.-W. Yeh, I.-C. Cheng, and J.-Z. Chen, Atmospheric pressure plasma jet processed reduced graphene oxides for supercapacitor application, J. Alloys Compd. **692**, 558 (2017).

[6] Y. Morabit, M. I. Hasan, R. D. Whalley, E. Robert, M. Modic, and J. L. Walsh, A review of the gas and liquid phase

interactions in low-temperature plasma jets used for biomedical applications, Eur. Phys. J. D **75**, 32 (2021).

[7] X. Lu, M. Laroussi, and V. Puech, On atmospheric-pressure non-equilibrium plasma jets and plasma bullets, Plasma Sources Sci. Technol. **21**, 034005 (2012).

[8] J. Li, B. Lei, J. Wang, B. Xu, S. Ran, Y. Wang, T. Zhang, J. Tang, W. Zhao, and Y. Duan, Atmospheric diffuse plasma jet formation from positive-pseudo-streamer and negative pulseless glow discharges, Commun. Phys. **4**, 64 (2021).

[9] X. Lu, G. V. Naidis, M. Laroussi, S. Reuter, D. B. Graves, and K. Ostrikov, Reactive species in non-equilibrium atmospheric-pressure plasmas: Generation, transport, and biological Effects, Phys. Rep. **630**, 1 (2016).

[10] Y. Duan, C. Huang, and Q. S. Yu, Cold plasma brush generated at atmospheric pressure, Rev. Sci. Instrum. **78**, 015104 (2007).

[11] J. Tang, S. Li, W. Zhao, Y. Wang, and Y. Duan, Development of a stable dielectric-barrier discharge enhanced laminar plasma jet generated at atmospheric pressure, Appl. Phys. Lett. **100**, 253505 (2012).

[12] A. Fridman, A. Chirokov, and A. Gutsol, Non-thermal atmospheric pressure discharges, J. Phys. D **38**, R1 (2005).

[13] H. Shiki, J. Motoki, H. Ito, H. Takikawa, T. Ootsuka, T. Okawa, S. Yamanaka, E. Usuki, Y. Nishimura, S. Hishida *et al.*, Development of split gliding arc for surface treatment of conductive material, Thin Solid Films **516**, 3684 (2008).

[14] J. Li, J. Wang, B. Lei, T. Zhang, J. Tang, Y. Wang, W. Zhao, and Y. Duan, A highly cost-efficient large-scale uniform laminar plasma jet array enhanced by V–I characteristic modulation in a non-self-sustained atmospheric discharge, Adv. Sci. **7**, 1902616 (2020).

[15] X. Li, J. Wu, B. Jia, K. Wu, P. Kang, F. Zhang, N. Zhao, P. Jia, L. Wang, and S. Li, Generation of a large-scale uniform plasma plume through the interactions between a pair of atmospheric pressure argon plasma jets, Appl. Phys. Lett. **117**, 134102 (2020).

[16] Z. Feng, N. Saeki, T. Kuroki, M. Tahara, and M. Okubo, Surface modification by nonthermal plasma induced by using magnetic-field-assisted gliding arc discharge, Appl. Phys. Lett. **101**, 041602 (2012).

[17] W. Jiang, J. Tang, Y. Wang, W. Zhao, and Y. Duan, A low-power magnetic-field-assisted plasma jet generated by dielectric-barrier discharge enhanced direct-current glow discharge at atmospheric pressure, Appl. Phys. Lett. **104**, 013505 (2014).

[18] B. Lei, B. Xu, J. Wang, X. Mao, J. Li, Y. Wang, W. Zhao, Y. Duan, V. Zorba, and J. Tang, Large modulation of ion dynamics for discharge-assisted laser-induced breakdown spectroscopy, Cell Rep. Phys. Sci. **4**, 101267 (2023).

[19] B. Xu, Y. Liu, P. Yin, M. Li, W. Zhang, Y. Wang, W. Zhao, J. Tang, and Y. Duan, Improving the laser-induced breakdown spectroscopy for highly efficient trace measurement of hazardous components in waste oils, Anal. Chem. **95**, 18685 (2023).

[20] Y. Liu, H. Qi, Z. Fan, H. Yan, and C. Ren, The impacts of magnetic field on repetitive nanosecond pulsed dielectric barrier discharge in air, Phys. Plasmas **23**, 113508 (2016).

[21] Y. Liu, H. Yan, H. Guo, Z. Fan, Y. Wang, and C. Ren, Experimental investigation on the repetitively nanosecond pulsed dielectric barrier discharge with the parallel magnetic field, Phys. Plasmas **25**, 023512 (2018).

[22] Y. Liu, H. Yan, H. Guo, Z. Fan, Y. Wang, Y. Wu, and C. Ren, Effect of parallel magnetic field on repetitively unipolar nanosecond pulsed dielectric barrier discharge under different pulse repetition frequencies, Phys. Plasmas **25**, 033519 (2018).

[23] B. L. Sands, B. N. Ganguly, and K. Tachibana, A streamer-like atmospheric pressure plasma jet, Appl. Phys. Lett. **92**, 151503 (2008).

[24] H. Kim, A. Brockhaus, and J. Engemann, Atmospheric pressure argon plasma jet using a cylindrical piezoelectric transformer, Appl. Phys. Lett. **95**, 211501 (2009).

[25] X. Lu and M. Laroussi, Dynamics of an atmospheric pressure plasma plume generated by submicrosecond voltage pulses, J. Appl. Phys. **100**, 063302 (2006).

[26] C. Zhang, T. Shao, Y. Zhou, Z. Fang, P. Yan, and W. Yang, Effect of O_2 additive on spatial uniformity of atmospheric-pressure helium plasma jet array driven by microsecond-duration pulses, Appl. Phys. Lett. **105**, 044102 (2014).

[27] C.-T. Liu, T. Kumakura, K. Ishikawa, H. Hashizume, K. Takeda, M. Ito, M. Hori, and J.-S. Wu, Effects of assisted magnetic field to an atmospheric-pressure plasma jet on radical generation at the plasma-surface interface and bactericidal function, Plasma Sources Sci. Technol. **25**, 065005 (2016).

[28] B. Shi, M. Wang, P. Li, R. Han, and J. Ouyang, Experimental investigation on atmospheric pressure plasma jet under locally divergent magnet field, Energies **16**, 2512 (2023).

[29] H. Xu, S. Guo, H. Zhang, and K. Xie, External axial magnetic field enhances discharge and water treatment of cold plasma jets, Appl. Phys. Lett. **119**, 054102 (2021).

[30] R. Safari and F. Sohbatzadeh, Effect of DC magnetic field on atmospheric pressure argon plasma jet, Indian J. Phys. **89**, 495 (2015).

[31] D. Breden and L. L. Raja, Computational study of the interaction of cold atmospheric helium plasma jets with surfaces, Plasma Sources Sci. Technol. **23**, 065020 (2014).

[32] W. Yan and D. J. Economou, Simulation of a non-equilibrium helium plasma bullet emerging into oxygen at high pressure (250–760 Torr) and interacting with a substrate, J. Appl. Phys. **120**, 123304 (2016).

[33] X. Y. Liu, X. K. Pei, X. P. Lu, and D. W. Liu, Numerical and experimental study on a pulsed-dc plasma jet, Plasma Sources Sci. Technol. **23**, 035007 (2014).

[34] D. Breden, K. Miki, and L. L. Raja, Self-consistent two-dimensional modeling of cold atmospheric-pressure plasma jets/bullets, Plasma Sources Sci. Technol. **21**, 034011 (2012).

[35] K. V. Laer and A. Bogaerts, Fluid modelling of a packed bed dielectric barrier discharge plasma reactor, Plasma Sources Sci. Technol. **25**, 015002 (2016).

[36] B. E. Poling, J. M. Prausnitz, and J. P. O'Connell, *The Properties of Gases and Liquids*, 5th ed. (McGraw-Hill, New York, 2001).

[37] A. Yu. Starikovskiy, N. L. Aleksandrov, and M. N. Shneider, Streamer self-focusing in an external longitudinal magnetic field, Phys. Rev. E **103**, 063201 (2021).

[38] T. A. van der Straaten, N. F. Cramer, I. S. Falconer, and B. W. James, The cylindrical DC magnetron discharge: I. Particle-in-cell simulation, J. Phys. D **31**, 177 (1998).

[39] G. J. M. Hagelaar and L. C. Pitchford, Solving the Boltzmann equation to obtain electron transport coefficients and rate coefficients for fluid models, Plasma Sources Sci. Technol. **14**, 722 (2005).

[40] Phelps Database, www.lxcat.net, retrieved on May 29, 2023.

[41] Biagi Database, www.lxcat.net, retrieved on May 29, 2023.

[42] Morgan Database, www.lxcat.net, retrieved on May 29, 2023.

[43] T. Murakami, K. Niemi, T. Gans, D. O'Connell, and W. G. Graham, Chemical kinetics and reactive species in atmospheric pressure helium-oxygen plasmas with humid-air impurities, Plasma Sources Sci. Technol. **22**, 015003 (2013).

[44] S. Rauf and M. J. Kushner, Dynamics of a coplanar-electrode plasma display panel cell. I. Basic operation, J. Appl. Phys. **85**, 3460 (1999).

[45] D. Liu, M. Rong, X. Wang, F. Iza, M. G. Kong, and P. Bruggeman, Main species and physicochemical processes in cold atmospheric-pressure He+O_2 plasmas, Plasma Process. Polym. **7**, 846 (2010).

[46] L. Wang, Y. Zheng, and S. Jia, Numerical study of the interaction of a helium atmospheric pressure plasma jet with a dielectric material, Phys. Plasmas **23**, 103504 (2016).

[47] Y. Jiang, Y. Wang, J. Zhang, S. Cong, and D. Wang, Numerical study on the production and transport of O and OH in a helium–humid air atmospheric pressure plasma jet interacting with a substrate, Phys. Plasmas **28**, 103501 (2021).

[48] W. Ning, D. Dai, Y. Zhang, Y. Han, and L. Li, Effects of trace of nitrogen on the helium atmospheric pressure plasma jet interacting with a dielectric substrate, J. Phys. D **51**, 125204 (2018).

[49] M. Altin, P. Viegas, L. Vialetto, G. J. van Rooij, and P. Diomede, Spatio-temporal analysis of power deposition and vibrational excitation in pulsed N_2 microwave discharges from 1D fluid modelling and experiments, Plasma Sources Sci. Technol. **33**, 045008 (2024).

[50] K.-M. Lin, Y.-H. Huang, W.-Y. Guo, and Y.-S. Chang, Development of a semi-empirical 1.5D plasma fluid model for a single microdischarge in atmospheric pressure dielectric barrier discharges, Plasma Sources Sci. Technol. **28**, 115014 (2019).

[51] T. Martens, A. Bogaerts, W. J. M. Brok, and J. V. Dijk, The dominant role of impurities in the composition of high pressure noble gas plasmas, Appl. Phys. Lett. **92**, 041504 (2008).

[52] Q. Wang, D. Dai, W. Ning, and Y. Zhang, Atmospheric dielectric barrier discharge containing helium–air mixtures: The effect of dry air impurities on the spatial discharge behavior, J. Phys. D **54**, 115203 (2021).

[53] B. Sun, D. Liu, X. Wang, Z. Liu, F. Iza, A. Yang, and M. Rong, Reactive species in cold atmospheric-pressure He+Air plasmas: The influence of humidity, Phys. Plasmas **26**, 063514 (2019).

[54] COMSOL Multiphysics version 5.3. (www.comsol.com). COMSOL AB, Stockholm, Sweden.

[55] Y. P. Raizer, *Gas Discharge Physics*, 1st ed. (Springer-Verlag, Berlin, 1991).

[56] D. W. Liu, F. Iza, and M. G. Kong, Electron heating in radio-frequency capacitively coupled atmospheric-pressure plasmas, Appl. Phys. Lett. **93**, 261503 (2008).

[57] G. V. Naidis, Modelling of plasma bullet propagation along a helium jet in ambient air, J. Phys. D **44**, 215203 (2011).

[58] K-U. Riemann, The Bohm criterion and sheath formation, J. Phys. D **24**, 493 (1991).

[59] H. Xu, L. Quan, Y. Liu, H. Zhang, M. Shao, and K. Xie, Effect of external $E \times E$ and $E \times B$ configurations on an atmospheric-pressure plasma jet and plasma-activated water: Experiments and simulations, Phys. Plasmas **29**, 073503 (2022).

[60] J. T. Hu, X. Y. Liu, J. H. Liu, Z. L. Xiong, D. W. Liu, X. P. Lu, F. Iza, and M. G. Kong, The effect of applied electric field on pulsed radio frequency and pulsed direct current plasma jet array, Phys. Plasmas **19**, 063505 (2012).

[61] X. Li, L. Nie, and X. Lu, Temporal electric field and electron density behavior of a He plasma jet with pulse width closing to pulse duration, Phys. Plasmas **30**, 033510 (2023).